REPORT DOCUMENTATION PAGE

Form Approved
OMB No. 0704-0188

1. AGENCY USE ONLY (Leave blank)	2. REPORT DATE 16 DEC 1994	3. REPORT TYPE AND DATES COVERED Final Technical 1 AUG 92 – 31 JUL 94

4. TITLE AND SUBTITLE
Basic Research in Nuclear Test Monitoring:
Seismic Wave Scattering from Irregular Interfaces

5. FUNDING NUMBERS
2309/AS
F49620-92-J-0413

6. AUTHOR(S)
Craig A. Schultz
Anton M. Dainty
M. Nafi Toksöz

7. PERFORMING ORGANIZATION NAME(S) AND ADDRESS(ES)
Massachusetts Institute of Technology
77 Massachusetts Avenue
Cambridge, MA 02139

8. PERFORMING ORGANIZATION REPORT NUMBER
60003

AFOSR-TR- 95 0042

9. SPONSORING/MONITORING AGENCY NAME(S) AND ADDRESS(ES)
AFOSR/NL
Building 410
Bolling Air Force Base DC 20332-6448
Dr. Stanley K. Dickinson

10. SPONSORING/MONITORING AGENCY REPORT NUMBER

DTIC
ELECTE
FEB 01 1995
S G D

11. SUPPLEMENTARY NOTES

12a. DISTRIBUTION/AVAILABILITY STATEMENT
Distribution Unlimited

12b. DISTRIBUTION CODE

13. ABSTRACT (Maximum 200 words).

We report on two investigations of seismic wave scattering from irregular interfaces. The first is a laboratory study of the scattering of ultrasonic waves incident on a glass surface etched to produce a highly irregular 3-D interface. We find that 2-D numerical simulations predict the 3-D experimental results well at small incident angles. Both numerical and experimental results strongly support the presence of enhanced backscattering. The second study is an analysis of regional P wave coda observed from events recorded at the Scandinavian NORESS, FINESA, and ARCESS arrays and the New England NYNEX array. The F-K spectra of the P coda are dominated by on-azimuth energy with apparent velocities between Pn (or faster) and Lg. Following this analysis, reflection coefficients calculated with a boundary integral scheme are used to study the role irregular interfaces play in the creation of regional P coda. We find that observed crustal scattering in these regions is strikingly consistent with P-P and P-SV scattering from the 2-D irregular Moho and even more consistent with scattering from a 2-D irregular near surface interface.

DTIC QUALITY INSPECTED 3

14. SUBJECT TERMS
Regional seismic monitoring, seismic scattering, P-wave coda, crustal interface scattering

15. NUMBER OF PAGES
76

16. PRICE CODE

17. SECURITY CLASSIFICATION OF REPORT	18. SECURITY CLASSIFICATION OF THIS PAGE	19. SECURITY CLASSIFICATION OF ABSTRACT	20. LIMITATION OF ABSTRACT
Unclassified	Unclassified	Unclassified	

NSN 7540-01-280-5500

AFOSR/NL

BASIC RESEARCH IN NUCLEAR TEST MONITORING: SEISMIC WAVE SCATTERING FROM IRREGULAR INTERFACES

Craig A. Schultz
Anton M. Dainty
M. Nafi Toksöz

Earth Resources Laboratory
Department of Earth, Atmospheric, and
  Planetary Sciences
Massachusetts Institute of Technology
Cambridge, Massachusetts 02139

Accesion For		
NTIS CRA&I		☒
DTIC TAB		☐
Unannounced		☐
Justification		
By _____		
Distribution /		
Availability Codes		
Dist	Avail and / or Special	
A-1		

16 December 1994

19950130 051

TABLE OF CONTENTS

List of Contributing Scientists

Anton M. Dainty, M.I.T. Visiting Scientist, Phillips Laboratory

Wenjie Dong, Graduate Research Assistant, Massachusetts Institute of Technology

Richard L. Gibson, Jr., Research Scientist, Massachusetts Institute of Technology

Batakrishna Mandal, Research Scientist, Massachusetts Institute of Technology

Chengbin Peng, Graduate Research Assistant, Massachusetts Institute of Technology

William Rodi, Research Scientist, Massachusetts Institute of Technology

Craig A. Schultz, Graduate Research Assistant, Massachusetts Institute of Technology

M. Nafi Toksöz, Professor of Geophysics, Massachusetts Institute of Technology

List of Previous and Related Contracts

Bibliography of Publications Totally or Partially Sponsored by the Contract

Schultz, C.A. and M.N. Toksöz, 1994, Experimental study of scattering from a highly irregular, acoustic-elastic interface, submitted to *J. Acoust. Soc. Am.*

Dainty, A.M. and C.A. Schultz, 1994, Crustal reflections and the nature of regional P coda, *Bull. Seism. Soc. Am.,* to appear.

Peng, C. and M.N. Toksöz, 1994, An optimal absorbing boundary condition for finite difference modeling of acoustic and elastic wave propagation, *J. Acoust. Soc. Am., 95,* 733–745.

Gibson, Jr., R.L., M.N. Toksöz, and W. Dong, 1994, Radiation from seismic sources in cylindrical cavities, Proceedings of the 16th Annual Seismic Research Symposium, Thornwood, New York, Air Force Phillips Laboratory, 113–119.

Toksöz, M.N., B. Mandal, W. Dong, and C. Schultz, 1993, Seismic scattering from non-spherical cavities and rough interfaces, Proceedings of the 15th Annual Seismic Research Symposium, Vail, Colorado, Air Force Phillips Laboratory, 405–411.

PREFACE

The objective of this research project is to understand phenomena of seismic wave generation and propagation that affect regional and teleseismic seismograms used for nuclear test monitoring. Two phenomena were investigated as part of this project: scattering by irregular interfaces, and the effect of non-sphericity of a cavity containing an explosion on its seismic wave radiation. Preliminary results on the latter topic have been reported in last year's annual techincal report and at the 15th Annual Seismic Research Symposium at Thornwood, New York. Our work on modeling the effects of non-spherical tunnels and cavities continues under an Air Force Office of Scientific Rersearch grant in progress, and final results of this work will be reported in future reports and publications.

This final report contains results of our invetigations of interface scattering. Under an earlier contract we reported the development of theoretical methods for modeling scattering from highly irregular interfaces. Here we report on the application of these methods to laboratory and field data. The first section of the report is a preprint of a paper submitted to the *Journal of the Acoustical Society of America*. It describes the results of ultrasonic laboratory experiments involving backscattering of acoustic waves from a glass surface etched to produce a highly irregular 3-D interface. The laboratory measurements are compared to numerical simulations performed with boundary element modeling. The second part of this report is a study of P wave coda observed at small aperture arrays in Scandinavia and New England from events at regional distances. The frequency-wavenumber characteristics of

the coda are analyzed and interpreted in terms of scattering from an irregular crust-mantle boundary or interfaces within the crust. This part of the report has been submitted for publication in the *Bulletin of the Seismological Society of America.*

EXPERIMENTAL STUDY OF SCATTERING FROM A

HIGHLY IRREGULAR, ACOUSTIC-ELASTIC INTERFACE

Summary

In this study, we experimentally and numerically develop statistical models for the scattering of an acoustic P wave which is incident on a highly irregular, random acoustic-elastic interface to determine the general nature of reflected energy. We then elucidate whether or not enhanced backscattering, already identified numerically for acoustic (SH) and fully elastic media (P-SV), occurs. Numerically, the problem is solved in two dimensions by coupling the representation theorem for an elastic medium with the extinction theorem. Exact integral expressions for the scattered pressure in the acoustic medium are then obtained, which include all converted and all multiply scattered waves at the boundary. Experimentally, a glass etching process using photoresist templates with Gaussian statistics allowed for the generation of characterized interface irregularities. Experiments were performed on a glass surface with an *rms* slope of 30 degrees, for the case of an incident wavelength with a size on the same order as the interface irregularities. The numerical models predict an enhancement of energy diffracted back towards the source, and results obtained in our in-house ultrasonic laboratory, strongly support the presence of this retroreflective energy. In terms of general scattering, we find that, at smaller incident angles (relative to vertical), the 2-D numerical results can give insight into the 3-D experimentally observed scattering over most scattering

angles. However, at larger incident angles, fundamental differences between 2-D and 3-D scattering may exist.

Introduction

In laboratory experiments, a lack of control over the statistical parameters of a given random model can easily produce ambiguous results. In the case of irregular interfaces, the height probability distribution and the correlation lengths of the interface may be poorly constrained, the interface statistics may show nonstationarity, and the interface may contain a wide variety of length scales. Each of these experimental uncertainties makes comparisons with numerical models difficult, if not impossible. It is the goal of this study to physically fabricate a random interface which is stationary in space, with both a simple probability distribution in height and a simple transverse correlation function. Experimental results can then be easily compared with the corresponding numerical results.

The accurate physical generation of a Gaussian surface is important experimentally, since Gaussian interfaces are mathematically convenient and have been widely used up to this point in scattering studies. Many theoretical formulations in the literature apply the simple properties of a Gaussian correlation function to heterogeneities. Examples can be found in Prange and Toksöz (1990), Knopoff and Hudson (1964, 1967), Haddon (1978), and Kuperman and Schmidt (1989). However, a Gaussian autocorrelation function is a somewhat unrealistic model for many regions of the earth since a Gaussian function is continuously differentiable

and has a rapid decay in spectral amplitude. This continuous differentiability and narrow wavenumber spectrum result in a very smooth model with one dominant length scale. More general fractal processes, which exhibit fluctuations on all length scales, are likely a more realistic model of true Earth structure. The most commonly utilized fractal representation is an exponential covariance function. In this case the model is continuous but not differentiable, making it a far rougher model than that given by the Gaussian function. The exponential covariance function has been utilized extensively, and in many instances gives a good description of physical properties (e.g., Wu and Aki, 1985; Frankel and Clayton, 1986). Recently, Goff and Jordan (1988) have generalized the exponential function. In this case, seafloor topography was modeled as a two-point covariance function with five free parameters which describe the amplitude, orientation, characteristic wavenumbers, and Hausdorff (fractal) dimension of the topography. These self-affine surfaces, of which the exponential covariance function is a special case, have been shown to give good first order stochastic descriptions of seafloor morphology.

As a first step at modeling scattering by irregular interfaces, we fabricate and physically model an irregular interface with a Gaussian correlation function. Upon evaluating the effectiveness of this experimental approach for the smoother Gaussian surface, more general, self-affine interface models may be proposed. In this study, the statistical parameters of the interface are chosen so that the incident wavelength has the same length scale as the correlation length of the irregularities. In addition, the *rms* slope of the interface is chosen to

be large, placing the model in a regime where approximate techniques such as the Kirchhoff, Born, and the geometrical ray approaches break down and multiple scattering mechanisms such as "enhanced backscattering" and "shadowing" play dominant roles.

What is "enhanced backscattering" from an acoustic-elastic halfspace? By definition, enhanced backscattering or "retroreflectance" is the enhancement of energy scattered back in the direction of the source. In optical theory, O'Donnell and Mendez (1987) were the first to propose the hypothesis that time-reversed paths are responsible for enhanced backscattering. This hypothesis was further strengthened by Maradudin *et al.* (1990) who showed that retroreflectance exists first for energy double scattered from an interface. Further support for this hypothesis came from the work of Schultz and Toksöz (1993,1994), which showed numerically that retroreflectance, which exists in the general case of seismic scattering, is consistent with the time-reversed path hypothesis. P-SV scattering gave the strongest support, as the hypothesis could be tested on various wave conversions at the interface. As predicted, energy enhancement was clearly observed on P-to-P and S-to-S scattering and not on P-to-S and S-to-P scattering.

The idea of time-reversed paths is easily extended to the acoustic-elastic case. Take for instance the peak-valley sequence shown in Figure 1. If an incident P-wave, shown by the solid line, diffracts from point 1 it will propagate as a P-wave to point 2 and then diffract at some angle into the upper medium again as a P-wave. For most waves traveling away from the interface, enhancement will not occur. However, if the diffracted wave travels

4

directly back towards the source, a plane wave component of incident P-wave can be found traveling exactly in the reverse direction: propagating from point 2 to point 1, and traveling back towards the source as shown by the dashed line. In this case, the time-reversed path interferes constructively with the forward path and contributes additional energy towards the source resulting in enhanced backscattering. Using a simple phase argument based on each of the studies cited above, some properties of enhanced backscattering can be derived. The peak width can be written as $\Delta\theta_s = \frac{\lambda}{l}$, where $\Delta\theta_s$ is the angular width of the peak, λ is the incident wavelength, and l is the mean free path of the interface or, in other words, the average distance a wave propagates between points 1 and 2 along the interface.

Adapting this phase approach, other path geometries may also contribute to enhanced backscattering. For example, if a wave encountering a 3-D irregular interface multiply scatters from several points outside the vertical source-receiver plane and then sends energy back in the direction of the source, then a time-reversed path may be found which also sends energy back towards the source. In the same manner, many multiply scattered paths, sending energy back towards the source, can be found in the acoustic-elastic case. However, as a result of energy loss with each diffraction from the interface, due to both transmission through the interface and additional spreading, it seems reasonable that the double-scattered paths, both in and out of the source-receiver (incident) plane, will contribute the majority of retroreflective energy.

Experimentally, there has been little investigation into coherent backscattering in the

acoustic case. However, for disordered acoustical systems, the recent study of Bayer and Niederdränk (1993) has shown that strongly heterogeneous media, such as random distributions of brass rods (2-D) and random distributions of gravel (3-D) can create weak localization effects. Coherent backscattering was studied in a narrow region about the backscattering direction where a simple diffusion model predicted the results well. Theoretical work has been done on the localization of acoustic waves, where Kirkpatrick (1985) has shown that all states are localized for dimension, $d \leq 2$. Although, this work may have implications for seismic scattering in an inhomogeneous crust, Condat and Kirkpatrick (1987) have shown that the localization of waves in an acoustic medium is very difficult to achieve unless extremely strong scatterers are present. Localization resulting from crustal heterogeneities, therefore, is likely far smaller than that resulting from interfaces.

This study is organized as follows. The first section briefly summarizes the numerical formulation used to model scattering from a randomly irregular acoustic-elastic interface. This Somigliana identity approach is an extension of the work of Schultz and Toksöz (1993,1994). In the second section, the physical construction of the characterized glass surface is discussed and the ultrasonic apparatus for measuring the amplitude distribution of energy scattered by the interface is described. The third section directly compares 3-D experimental results obtained in our in-house ultrasonic water tank with the corresponding 2-D numerical results. Amplitude distributions are presented in detail and scattering mechanisms are proposed. Finally, we investigate the differences between the 2-D synthetic and the 3-D experimental

data and discuss the implications for both 2-D and 3-D scattering mechanisms.

Theory

The numerical approach and notation in this section follows that of Schultz and Toksöz (1993, 1994). Since the approach here is very similar to the SH and P-SV cases, we give only a brief outline of the theoretical approach. We first express the total scattered displacement at any point within two volumes of elastic material with the Somigliana representation theorem (e.g., Aki and Richards 1980). Simplifying this theorem to a 2-D case gives the following integral equations

$$
\begin{aligned}
H[l]u_n^{(l)}(\underline{x}) = {} & \int_V f_p^{(l)}(\underline{\eta})G_{np}^{(l)}(\underline{x};\underline{\eta})dV(\underline{\eta}) \\
& + \int_S dS(\underline{x}')\{[c_{ijpq}^{(l)}\hat{n}_j(\underline{x}')\partial G_{np}^{(l)}(\underline{x};\underline{x}')/\partial x_q']u_i^{(l)}(\underline{x}') \\
& - G_{np}^{(l)}(\underline{x};\underline{x}')T_p^{(l)}(\underline{u}^{(l)}(\underline{x}'),\hat{n})\},
\end{aligned}
\tag{1}
$$

where gradients are zero in the x_2-direction. Following the notation of Schultz and Toksöz (1993), $T_p^{(l)}(\underline{x})$ is the traction vector along the interface in both the fluid ($l = f$) and the solid ($l = s$), and we have assumed all surfaces to be far enough away so that only the surface, $S(\underline{x})$, separating the two volumes, contributes to the final displacement. $G_{np}(\underline{x};\underline{x}')$ is a Green's function giving the n-component of displacement at $\underline{x}$ resulting from a point force in the p-direction at $\underline{x}'$, c_{ijpq} is the elasticity tensor, and $H[i]$ is a function that takes a value of 0 or 1 depending on whether the point $\underline{x}$ lies outside or inside the volume of interest,

l, respectively. We assume that the media are homogeneous and isotropic.

In this work the upper medium is acoustic, supporting propagation of only dilatational waves, while the lower medium is taken to be elastic. The boundary conditions for the resulting acoustic-elastic boundary, can be written in the general form

$$\underline{n} \cdot \underline{u}^{(f)}(\underline{x})|_{x_3=\zeta(x_1)} = \underline{n} \cdot \underline{u}^{(s)}(\underline{x})|_{x_3=\zeta(x_1)},$$

$$\underline{\underline{T}}^{(f)}(\underline{x})|_{x_3=\zeta(x_1)} = \underline{\underline{T}}^{(s)}(\underline{x})|_{x_3=\zeta(x_1)}, \tag{2}$$

$$\underline{n} \times \underline{\underline{T}}^{(s)}(\underline{x})|_{x_3=\zeta(x_1)} = 0,$$

where the surface profile function is taken to be $x_3 = \zeta(x_1)$ and the unit normal vector along the interface can be written as

$$\hat{n} = (-\zeta'(x_1), 1)[1 + (\zeta'(x_1))^2]^{-\frac{1}{2}}. \tag{3}$$

The first boundary condition in (2) represents the continuity of normal displacement and the other two conditions together represent the continuity of normal stress.

Taking our volume of interest to be the upper acoustic medium, placing the incident wave in the acoustic medium, substituting the final form of the boundary conditions (2), and letting $x_3 \to \zeta^+(x_1)$, the final set of coupled integral equations can be written as

$$S(\underline{x}) = S^{(f)}(\underline{x})_{incid} \tag{4}$$

$$+ \int_{-\infty}^{+\infty} dx_1' [S(\underline{x}')T^{(f)}(\underline{x}|\underline{x}') - D_n^{(f)}(\underline{x}|\underline{x}')D_n(\underline{x}')],$$

in the acoustic medium, and

$$0 \; = \; -\int_{-\infty}^{+\infty} dx'_1 [U_i(\underline{x}')T_i^{n(s)}(\underline{x}|\underline{x}') - \frac{\lambda^{(f)}}{\mu^{(s)}}D_n^{(s)}(\underline{x}|\underline{x}')S(\underline{x}')], \tag{5}$$

in the elastic medium, where we have defined

$$T^{(f)}(\underline{x}|\underline{x}') \; = \; \lambda^{(f)}\frac{\partial G^{(f)}(\underline{x};\underline{x}')}{\partial n}\big|_{x_3=\zeta(x_1)}, \tag{6}$$

$$D_i^{(f)}(\underline{x}|\underline{x}') \; = \; -\lambda^{(f)}k_t^{(f)2}G^{(f)}(\underline{x};\underline{x}')n_i\big|_{x_3=\zeta(x_1)},$$

$$T_i^{n(s)}(\underline{x}|\underline{x}') \; = \; T_i^{n(s)}(\underline{x}|\underline{x}')\big|_{x_3=\zeta(x_1)},$$

$$D_n^{(s)}(\underline{x}|\underline{x}') \; = \; \mu^{(s)}G_{np}^{(s)}(\underline{x};\underline{x}')n_p\big|_{x_3=\zeta(x_1)}.$$

in the respective media. Now the unknown source strength functions, which we eventually

solve for, can be expressed as a function of x_1 alone

$$S(x_1) \; = \; \theta^{(f)}(\underline{x})\big|_{x_3=\zeta(x_1)}, \tag{7}$$

$$D_i(x_1) \; = \; U_i^{(f)}(\underline{x})\big|_{x_3=\zeta(x_1)},$$

where $\theta(\underline{x}) = u_{k,k}(\underline{x})$ is the dilatational parameter, λ and μ are the Lamé parameters for the

medium, $\underline{U}(\underline{x})$ is the displacement along the interface, where $S^{(f)}(\underline{x})$ should not be confused

with the surface function referred to previously. The pressure term has been normalized

with respect to $\lambda^{(f)}$ to ensure that the final numerical system is well conditioned.

We now approximate the transducer source as a narrow Gaussian beam source (Schultz

and Toksöz, 1993). This beam source acts to dramatically reduces the computational demand

of this numerical approach, since only a small portion of the interface is excited by the

9

incident beam and the length of integration along the acoustic boundary is reduced. The half width of the incident beam is $w = h \cos \theta_0$, where h is the half–width of the incident beam as projected on the plane $x_3 = 0$. The scattered field in the acoustic medium can now be expressed completely in terms of the unknown source functions. Substituting the Cartesian form of the Green's functions for a homogeneous halfspace (Bouchon and Aki, 1977), the scattered pressure at any point, $x_3 > \zeta(x_1)_{max}$, in the fluid can be decomposed into a summation of plane waves.

An approximation to the Fourier reflection coefficient can now be written in terms of an amplitude coefficient by normalizing the scattered wave amplitude coefficient by the amplitude of the incident plane wave component having a wavenumber vector corresponding to the angle of incidence. The reflection coefficient can then be expressed as

$$R(k\omega) = \frac{|r_p(\theta_s)|}{2\sqrt{\pi} k_t^{(f)} w}, \tag{8}$$

where

$$r_p(\theta_s) = \int_{-\infty}^{+\infty} dx_1' [iS(x_1') k_t^{(f)} (\sin\theta_s \zeta(x_1') - \cos\theta_s) \tag{9}$$
$$- k_t^{(f)2}(\zeta'(x_1') D_1(x_1') - D_3(x_1'))] e^{-ik_t^{(f)}(\sin\theta_s x_1' + \cos\theta_s \zeta(x_1'))},$$

which is comparable in amplitude to the Fourier reflection coefficient calculated for a single incident plane wave. This normalization is different from the Differential Reflection Coefficient implemented by Schultz and Toksöz (1993,1994). Note that we let $k = k_t^{(f)} \sin\theta_s$ and $k_z = k_t^{(f)} \cos\theta_s$.

10

These integral equations can now be solved numerically. The solution over an acoustic-elastic interface can be expressed completely as a combination of the Green's functions for the P-SV and SH cases (Schultz and Toksöz, 1993, 1994), where the shear velocity of the SH wave is changed to the P-wave velocity of the acoustic medium, so as to reflect the acoustic Green's function. The final coupled integral equations are then transformed to a coupled set of matrix equations and solved using LU decomposition or biconjugate gradient techniques.

In this paper two types of interfaces are modeled numerically. Both interfaces have a Gaussian distribution about the mean, where $\delta^2 = \langle \zeta^2(x_1) \rangle$ is the mean-square departure of the surface from flatness. The first interface studied has a correlation function

$$W(|x_1 - x_1'|) = \delta^{-2} \langle \zeta(x_1) \zeta(x_1') \rangle, \tag{10}$$

described by the Gaussian function, $W(|x_1|) = exp(-x_1^2/a^2)$. The correlation length, a, for a Gaussian interface is approximately equal to the average distance between adjacent peaks and valleys along the interface. The interface can also be described in terms of the *rms* slope of the surface, ϕ, which we will refer to often. This *rms* slope can be written as $\phi = tan^{-1}(\frac{\sqrt{2}\delta}{a})$. The second surface studied has an exponential correlation function, $W(|x_1|) = exp(-x_1/a)$.

Averaging over an ensemble of realizations of these surfaces, we display the final scattered pressure as a statistical average that follows the approach of Schultz and Toksöz (1993,1994). The total mean squared contribution to the reflection coefficient (RC) can then be written

as

$$\langle\frac{\partial R_p}{\partial \theta_s}\rangle_{tot} = \frac{4\pi}{k_t^{(f)2}w^2}\langle|r_p(\theta_s)|^2\rangle. \tag{11}$$

This gives the average square pressure reflected into the upper medium as a function of the scattering angle, θ_s, given one incident beam angle, θ_0. The square root of the RC is used for comparison with experimentally recorded amplitudes. Given this representation, a Gaussian beam which is perfectly reflected by a plane interface gives a maximum reflection coefficient value of one.

Experimental Procedure

The experimental approach consists of submerging a solid elastic model, in this case a glass block, into an experimental water tank, thus creating an acoustic-elastic interface. More precisely, this experiment involved the generation of an interface with a characterized random surface and the design of a measurement configuration that could accurately, to within a fraction of a degree, measure various realizations of the fluid-glass boundary.

Random Interface Generation

Fabricating the randomly irregular surface was the most challenging part of this project. Numerous irregular surfaces were designed. Models ranged from irregular distributions of glass beads to roughened cement surfaces. In addition, random distributions of gravel held together by epoxy were tested along with naturally rough granite and sandstone surfaces.

Unfortunately, these models either did not give proper control over statistical parameters or were extremely heterogeneous at the ultrasonic level, making comparisons with numerical models very difficult. After much experimentation the most promising approach became the fabrication of a random glass surface using an etching procedure.

The irregular glass surface was designed using a solid glass block and a standard glass etching process. First a cylindrical glass block with a diameter of 19.5 cm and a height of 7.5 cm was cast using a graphite mold. Then to achieve the desired random interface, the Gaussian surface described in the previous section was first numerically generated. The transverse correlation length, a, and the standard deviation of the height, δ, of the interface were specified as 1 mm and .71 mm, respectively, giving an *rms* slope of 45°. After its numerical generation, the Gaussian surface was discretized into six individual depth levels, with each level's thickness equal to one standard deviation of the interface height, δ. The templates, shown in Figure 2, were successively glued to the surface and each template was exposed to high velocity sand particles normally incident on the surface. As a result, the desired interface was etched in six discrete depth intervals. In general, the correlation length of the surface was controlled by the template design and the standard deviation of the interface was controlled by the time that each template was exposed to the sand blast.

The Scattering Instrumentation

Once the irregular glass surface was created, an automated scattering apparatus was used to measure the scattering properties of the interface. Two different flat-sub-bottomed transducers were used to create a beam source. They consisted of a Panametrics 12.7 mm diameter transducer (1.5 MHz, $\lambda = 1.0$ mm in water) and a Panametrics 25.4 mm diameter transducer (0.5 MHz, $\lambda = 3.0$ mm in water). The detectors, which were also Panametrics flat-sub-bottomed transducers, consisted of a 6.4 mm diameter transducer (1.5 MHz, $\lambda = 1.0$ mm in water) and a 12.7 mm diameter transducer (0.5 MHz, $\lambda = 3.0$ mm in water), respectively. The detectors were chosen such that they were sensitive only to waves approaching nearly perpendicular to the bottom surface of the transducer, limiting the energy recorded to waves approaching in line with the transducer axis. Given the source parameters, the resulting source radiation pattern was a beam with most of the energy traveling in the forward direction. The source radiation patterns exhibited some slight spreading of the beam, although further tests showed that this did not significantly affect the results.

The experimental geometry used to measure the scattered amplitudes is shown in Figure 3. The glass block was located at the center of the experiment and the source and detector were then stepped in a semicircle about an axis of rotation. This axis extended laterally along the irregular fluid-glass interface and perpendicular to the source-receiver plane. In each experiment the source was placed at a constant incident angle, θ_0, and a constant .35 m distance from the axis of rotation. The recording angle was then controlled by mounting

the detector on a motor–driven, rotating arm that held the detector .30 m from the given axis of rotation. The arm was then rotated in 0.9° steps about this axis of rotation. Therefore, the recorded energy represents scattering in the plane of incidence. Unfortunately, the detector occludes the source when it is near the backscattering position, resulting in a loss of 3° to 6° of measurements near the source position. These data points are not plotted.

The final measurement is the mean scattered pressure as a function of scattering angle, given a fixed angle of incidence. The scattered pressure is measured at specific frequencies by introducing directly via the transducer source a monochromatic wave of a given frequency. The continuous wave is approximated by a finite sinusoid ranging between 35 and 100 cycles and the final constant amplitude of the scattered pressure is recorded. Since for a single realization, the waves scattered from an irregular interface exhibit large fluctuations in pressure as a function of the scattering angle, the experimental data was averaged to obtain a final mean reflection coefficient. To this end, a simple scheme was developed to generate many realizations using the same 3-D sample. In general, each realization was acquired by rotating and shifting the sample in a prechosen sequence. In general, the sample was rotated by 60° staggered steps, followed by 1.25 cm lateral shifts of the block relative to the measuring devices. Since rotating the surface with respect to the incident beam formed another scattering geometry, many different realizations of the interface were obtained.

As a result of our interest in the enhancement of energy traveling directly back towards the source, a receiver was created that could retrieve energy in the occluded zone near the source.

This was achieved by constructing a piezofilm receiver, which had an impedance similar to that of water, therefore, allowing the source beam to propagate through it with minimal distortion. More precisely, a four-layered, in-parallel piezofilm receiver was constructed to allow for a significant increase in the signal to noise ratio.

The data presented in the next section represents the mean diffusely scattered signal, as a function of angle, for a fixed solid angle of data acquisition. No artificial angular factors are introduced to the data. For comparison, the data is normalized by the numerical RC calculated at normal incidence.

Surface Scattering Measurements

In this section we present the average reflection coefficients obtained over the roughest glass surface fabricated, thus allowing a study of the strongest form of scattering at an irregular interface. Figure 4a shows the target surface height distribution for this interface, independent of lateral position, and Figure 4b shows the histogram of the surface height, based on surface profilometer measurements of the actual surface. The surface measurements have a lateral resolution of about 5 μm, which is within the range of accuracy required for resolving the interface statistics. These histograms show that the surface follows approximately a Gaussian probability distribution with a standard deviation of about 0.6 mm, which is close to the target value of 0.71 mm. Figure 5a gives the target Gaussian autocorrelation function, and Figure 5b shows the the actual autocorrelation function calculated from pro-

filometer measurements. The correlation length of 1.4 mm is greater than the target value of 1 mm. Also plotted are the Gaussian and exponential autocorrelation functions with the same correlation length as the data. The measured autocorrelation function is very close to a Gaussian correlation function at the more important, smaller lag distances. At larger lag distances, the surface lies directly between a Gaussian and an exponential correlation function.

Figure 6a gives a grayscale plot of the experimental surface based on surface profilometer measurements. Figure 6b plots the surface height for a profile taken across the surface, while Figure 6c shows a numerically generated Gaussian and exponential surface given the same standard deviation and correlation length. The etching process, being a natural process, not surprisingly tends towards a rougher interface with a broader power spectrum than the targeted Gaussian spectrum. However, even with these deviations, it is clear upon referring to Figure 6c that the Gaussian surface matches the experimental interface well, in both the observed slopes and the lateral scale of the irregularities. Although the Gaussian interface gives a good fit to the experimental data, out of interest we shall also include the numerical results for an exponential surface.

Based on the measurements above, the final glass interface has approximately a 30° rms slope. The slopes of this interface are quite steep and the impedance contrast at the fluid-glass interface is large as the glass interface has properties very similar to those of an igneous material. As a result, multiple-scattering and shadowing effects can play a significant role

at both small and large incident angles, and approximate linear theories, such as the Kirch-hoff and Born approaches, break down. Therefore, the mean scattered pressure measured experimentally is compared with the reflection coefficients calculated with the Somigliana boundary integral technique, as this numerical approach includes all multiple scattering and wave conversions at the interface.

Case: $\lambda = 0.71a$

Figure 7 shows one realization of the interface given an incident pulse with a center frequency of 1.5 MHz and a half-power width of 0.25MHz. This realization corresponds to a beam impinging on the surface with an incident angle of 20°. The source pulse along with the pulse reflected from a plane interface are also shown, in which case energy travels only in the specular direction. Referring to the polar seismogram, it is clear that the large scale surface roughness scatters energy over most forward and back scattering angles. The energy is spread over a large time interval and amplitudes vary rapidly as a function of scattering angle. In general, it is difficult, given this single model, to determine quantitatively which scattering mechanisms are working at the surface.

Our first continuous wave analysis is carried out at 1.5 MHz, the center frequency of the seismogram above, so that $\lambda = .71a = 1.00$ mm. If one were to look at a single experimental realization of the fluid-glass surface at each of four incident beam angles: 0°, 20°, 30°, and 60° one would find that the amplitudes in each realization vary strongly as a function of

scattering angle, θ_s. Averaging over a finite number of these realizations the mean reflection coefficient is obtained. The total mean reflection coefficients for both a Gaussian and an exponential surface are given in Figures 8 through 11.At the bottom of these figures, the experimental mean reflection coefficients are given along with the SD of the finite average, showing the deviation of these reflection coefficients from the final mean reflection coefficient, which would correspond to a full ensemble of realizations. Negative scattering angles ($\theta_s < 0$) correspond to backscattering in all plots. We also stress that given the incident wavelength, the surface is extremely irregular and the specular reflection is largely disrupted.

Figure 8 shows the total mean scattered pressure as a function of scattering angle given a normally incident acoustic beam. Upon comparing the numerical and experimental data it is clear that the 2-D numerical results for a Gaussian interface can give insight into the 3-D experimental results. The fluctuations in the data are mostly within one standard deviation of the finite average. There are a number of interesting aspects in the curves. The experimental data shows a strong peak amplitude propagating back towards the source at $\theta_s = 0°$, and this is predicted by the numerical reflection coefficient. The width of this peak is approximately 35°. Notice that there is also considerable scattering at all angles, dropping off linearly with increasing scattering angle. The exponential surface also predicts portions of the amplitude distribution, but its higher frequency component appears to destroy the enhancement of energy scattered back towards the source.

A similar form of scattering is exhibited in Figures 9 and 10, which show the mean

scattered pressure for an incident angle of 20° and 30°, respectively. Again the numerical results for the Gaussian interface are similar in nature to the experimental results. There are also some remarkable aspects to these two curves. First, both reflection coefficients contain two dominant peaks. One peak is broad and occurs in the forward scattered direction while the other peak is much narrower and occurs in the retroreflective direction, $\theta_s = -\theta_0$. The experimental results show a consistent, yet less distinct, peak in the retroreflective direction. This peak clearly loses amplitude as the incident angle is increased, sinking further into the surrounding reflection coefficient. A second aspect is that both curves show a strong asymmetry. However, upon comparing the curves, the 2-D numerical model shows more backscattering and less forward scattering than the 3-D ultrasonic data. This trend becomes more prominent as the incident angle is increased. The exponential curve follows the Gaussian reflection coefficient closely, although it again shows a less distinct retroreflective peak.

Figure 11 gives the mean scattered pressure for a beam incident at 60°. In this case there are no distinct signs of enhanced backscattering in either the numerical or the experimental data. However, energy is scattered uniformly over most backscattering angles. This energy does not drop off until the retroreflective angle is exceeded in the backscattering region. Most dramatic is the continuation of the trend observed at the smaller incident angles above. Specifically, the numerical data clearly shows a slower falloff in backscattering and a slower rise in forward scattering than exhibited by the 3-D experimental data.

Case: $\lambda = 2.14a$

Figure 12 shows one realization of the interface given an incident pulse with a center frequency of 0.5 MHz and a half-power width of 250 kHz. This realization corresponds to a beam impinging on the surface at a 20° incident angle. The pulse reflected from a plane interface is shown, with the energy again arriving only in the specular direction. Referring to the scattered seismogram, it is clear that, even at this lower frequency, energy is scattered over most forward and backscattered angles. Given this one deterministic case, it is again difficult to determine quantitatively the scattering mechanisms operating at this frequency.

The second continuous wave analysis was carried out at 0.5 MHz, the center frequency of the seismogram above, so that $\lambda = 2.14a = 3.0$ mm. Once again, if one were to look at a single realization, the amplitudes for each realization vary strongly as a function of scattering angle, although not as strongly as the $\lambda = .71a$ case. Figure 13 shows the comparison between the numerical and experimental mean reflection coefficients given a normally incident beam. The 2-D numerical results for a Gaussian interface are able to predict portions of the experimental observations. In this case, much of the experimental data sits within one standard deviation of the finite-average. Comparing these curves to the curves for $\lambda = 0.71a$, a number of distinct differences are apparent. Most noticeable is the widening of the retroreflective peak width from about 35° to greater than 60°. This widening is apparent in both the experimental and the numerical data. The reflection coefficient for an exponential interface again shows much lower retroreflectance than for the Gaussian interface.

Figures 14 and 15 both show that the numerical results over a Gaussian interface predict the asymmetric trends in the experimental data for incident angles of 20° and 30°, respectively. However, distinct differences do occur between the two curves. First, as the incident angle increases, the 2-D numerical results again show more backscattering and less forward scattering than the 3-D ultrasonic data. A broad retroreflective peak is both predicted and observed at 20° and 30° incidence, supporting the existence of retroreflectance. Unfortunately, the height of these peaks are of the same order as the standard deviation of the experimental average, not allowing for a direct verification of retroreflectance. Numerically, the exponential interface does give rise to a retroreflective peak, although this peak is smaller than the peak predicted by the Gaussian surface.

Figure 16 shows the mean reflection coefficient for an incident angle of 60°. In this case enhanced backscattering is not predicted numerically or observed experimentally. The 2-D numerical model again predicts a slower falloff in backscattering and a slower rise in forward scattering than exhibited by the 3-D ultrasonic data. In addition, the numerical model predicts a much smaller specular peak than is observed experimentally. Although the amplitudes are different, the numerical curves do predict the uniform scattering of energy into the fluid above as shown in the data.

Retroreflectance is clearly supported by the ultrasonic data above. However, the retroreflective peak height is still on the same order as the standard deviation of the finite-average in each case. This makes it difficult to verify the existence of "enhanced backscattering"

absolutely. For this reason, data was recorded near the retroreflective direction using the partially transparent piezofilm receiver. The final average RC observed with the piezofilm receiver is superposed on Figure 14. The data has been scaled to the amplitudes received with the flat–bottomed transducers. The scattered pressure was measured between the backscattering angles of 40° and 5° ($-40° < \theta_s < -5°$), and 65 surface realizations were averaged. In this case, a distinct peak is observed in the retroreflective direction with a slightly narrower form than the numerically generated peak. The size of the retroreflective peak is larger than the corresponding SD of the average, strongly supporting the the presence of an enhancement of retroreflected energy due to multiple scattering from the glass interface.

Upon a careful review of the numerical and experimental curves above there are finer features in the experimental data which may be of importance. For instance, the experimental observations show a distinct change in the variance of the amplitude measurements. In the both the $\lambda = 2.14a$ and the $\lambda = .71a$ case, the variance of the mean reflection coefficient decreases dramatically outside the $-60° < \theta_s < +60°$ range. This change in variance does not appear to depend strongly on the incident angle or the incident wavelength, at least in the frequency range studied. The change occurs in conjunction with a sharp break and a distinct drop in the reflected amplitudes at wider scattering angles, suggesting that it may be associated with shadowing effects at the larger scattering angles. Numerically, by averaging a similar number of 2-D numerical realizations, this break in the variance for a small finite average can be predicted. As more realizations are averaged, the sharpness

23

of the break in reflected amplitudes becomes smoothed. Surprisingly, the model with an exponential correlation function predicts the point of this break better than the Gaussian model.

Upon comparing the experimental and numerical curves, additional discrepancies can be identified between the numerically predicted and the experimentally observed amplitudes. The most prominent discrepancy is the appearance of a large amplitude specular peak at small incident angles in the 3-D data. While a peak is clearly present in the specular direction by a 20° incident angle in the each 3-D case, a distinct specular peak is only present for $\theta_0 = 30°$ in the $\lambda = 2.14a$ numerical case. Discrepancies such as this can be useful for understanding the effect of 2-D and 3-D structures on seismic motions.

Discussion and Conclusions

In this study, we were able to generate, within reasonable accuracy, a 3-D characterized random interface. An interface with approximately a Gaussian surface height distribution and a Gaussian correlation function was generated using a glass etching procedure and photoresist templates. The resulting surface distribution was confirmed using surface profilometer measurements. Scattered pressures were then acquired over this surface and compared directly to numerical results for a 2-D interface with the same statistical parameters.

Generally, the numerically derived mean reflection coefficients calculated over an acoustic-elastic interface show retroreflective trends similar to those observed for the SH and P-SV

cases. First, the width of the retroreflective peak appears to be consistent with the multiple scattering, constructive phase argument summarized in the introduction. In this case, when the wavelength is increased, both the numerically derived curve and the experimental data show an increase in peak width, from $35°$ at $\lambda = .71a$, to greater than $60°$ at $\lambda = 2.14a$. Second, as the incident angle is increased, the retroreflective peak amplitude tends to decrease relative to the remaining portion of the reflection coefficient. The retroreflective peak in both the experimentally and numerically derived curves disappears at an incident angle approximately equal to the $30°$ *rms* slope of the interface. Finally, although not studied directly, it seems likely, based on the work of Schultz (1993), that the retroreflective peak height will tend to decrease as the impedance contrast is lowered and more energy is allowed to penetrate the interface. Along the same lines, the retroreflective peak amplitude is likely to diminish as the *rms* slope of the interface is decreased, since not as many time-reversed paths can be obtained with the lower slopes.

Near normal incidence, we have shown that the 2-D numerical results for scattering from a randomly irregular interface, with Gaussian statistics, can give insight into the 3-D scattering observed experimentally. At larger incident angles, the 2-D numerical curves deviated from the experimental curves significantly. More specifically, as the incident angle was increased to greater than $20°$, the 2-D models predicted a slower decrease in backscattering and a slower increase in forward scattering than observed in the 3-D experimental data. The trend became dramatic as the incident angle was increased to $60°$. Since the surface in this experiment was

25

well characterized, this appears to be the result of inherent differences between 2-D and 3-D scattering mechanisms. More precisely, as the incident angle is increased the extra degree of spatial freedom associated with a 3-D interface appears to favor the propagation of more forward scattered energy and less backscattered energy relative to a 2-D interface. Although the falloff in amplitudes was different between the 2-D and 3-D interfaces, the 2-D numerical results did predict the general trend of the experimental scattering. Both results showed that at large incident angles energy is scattered uniformly over most scattering angles, resulting in negative phase velocities, large phase velocities, and a large amount of interference in seismic data recorded in the fluid above.

Although tests were not carried out on epoxy surfaces in this study, an epoxy surface was generated for the purpose of profilometer measurements, by using the irregular glass surface as a mold. Future work may, therefore, include studies to determine how material properties affect scattering from surfaces with identical height distributions. Also, a similar etching process may be used to study interfaces with differing statistics.

Acknowledgements

References

Abramowitz, M. and Stegun, I.A., 1964, *Handbook of Mathematical Functions*, Dover Publications, New York, NY (sections 9.1.3,9.1.10–11,9.1.27,9.1.30,9.4.1–6).

Bayer, G., and Niederdränk, T., 1993, Weak localization of acoustic waves in strongly scattering media, *Phys. Rev. Let., 70*, 3884–3887.

Condat, C.A., and Kirkpatrick, T.R., 1987, Observability of acoustical and optical localization, *Phys. Rev. Let., 58*, 226–229.

Frankel, A., and Clayton, R., 1986, Finite difference simulations of seismic scattering: implications for the propagation of short-period seismic waves in the crust and models of crustal heterogeneity, *J. Geophys. Res., 91*, 6465–6489.

Goff, J.A., and Jordan, T.H., 1988, Stochastic modeling of seafloor morphology: inversion of sea beam data or second-order statistics, *J. Geophys. Res., 93*, 13,589–13,608.

Haddon, R.A.W., 1978, Scattering of seismic body waves by small random inhomogeneities in the earth, *NORSAR Sci. Rep., 3-77/78*, Norw. Seismic Array, Oslo.

Kirkpatrick, T.R., 1985, Localization of acoustic waves, *Phys. Rev. B, 31*, 5746–5757.

Knopoff, L., and Hudson, J.A., 1964, Scattering of elastic waves by small inhomogeneities, *J. Acoust. Soc. Am., 36*, 338–343.

Knopoff, L., and Hudson, J.A., 1967, Frequency dependence of amplitudes of scattered elastic waves, *J. Acoust. Soc. Am., 42*, 18–20.

Kuperman, W.A., and Schmidt, H., 1989, Self-consistent perturbation approach to rough

scattering in stratified media, *J. Acoust. Soc. Am., 86*, 1511–1522.

Maradudin, A.A., Michel, T., McGurn, A.R., and Méndez, E.R., 1990, Enhanced backscattering of light from a random grating, *Annals of Physics, 203*, 255–307.

O'Donnell, K.A. and Méndez, E.R., 1987, Experimental study of scattering from characterized random surfaces, *J. Opt. Soc. Am., 4* , 1194–1205.

Prange, M., and Toksöz, M.N., 1990, Perturbation approximation of 3-D seismic scattering, *Geophys. J. Int., 101*, 713–738.

Schultz, C.A. and Toksöz, M.N., 1993, Enhanced backscattering of seismic waves from a highly irregular interface: SH case, *Geophys. J. Int., 114*, 91–102.

Schultz, C.A. and Toksöz, M.N., 1994, Enhanced backscattering of seismic waves from a highly irregular interface: P-SV case, *Geophys. J. Int., 117*, 783–810.

Wu, R., and Aki, K., 1985, Scattering characteristics of elastic waves by an elastic heterogeneity, *Geophysics, 50*, 582–595.
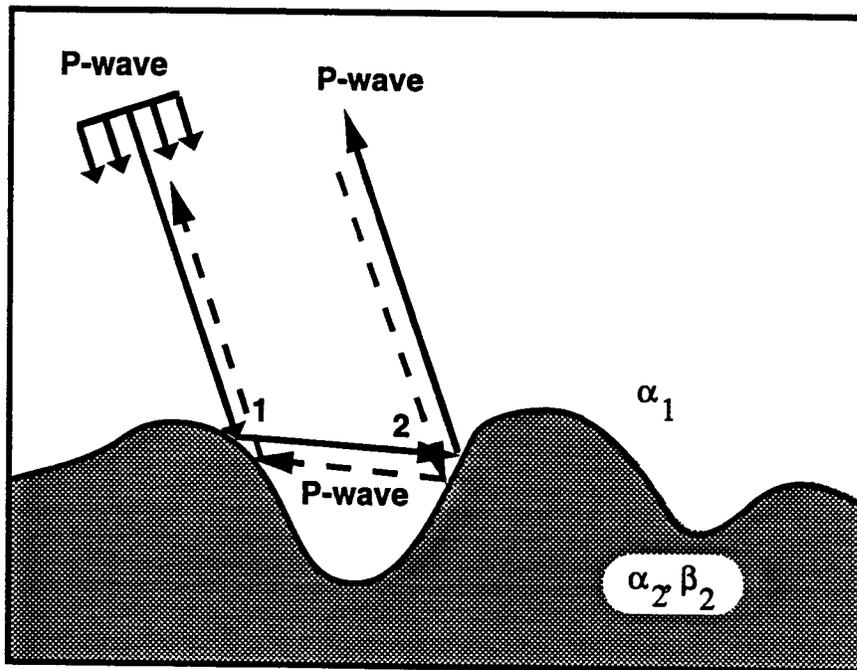
Figure 1: Peak-valley sequence along an interface showing an example of the time-reversed paths which lead to enhanced backscattering. The solid line shows a forward scattered path while the dashed line shows the corresponding time-reversed path. These two paths interfere constructively to give an increase in amplitude diffracted back in the direction of the source.
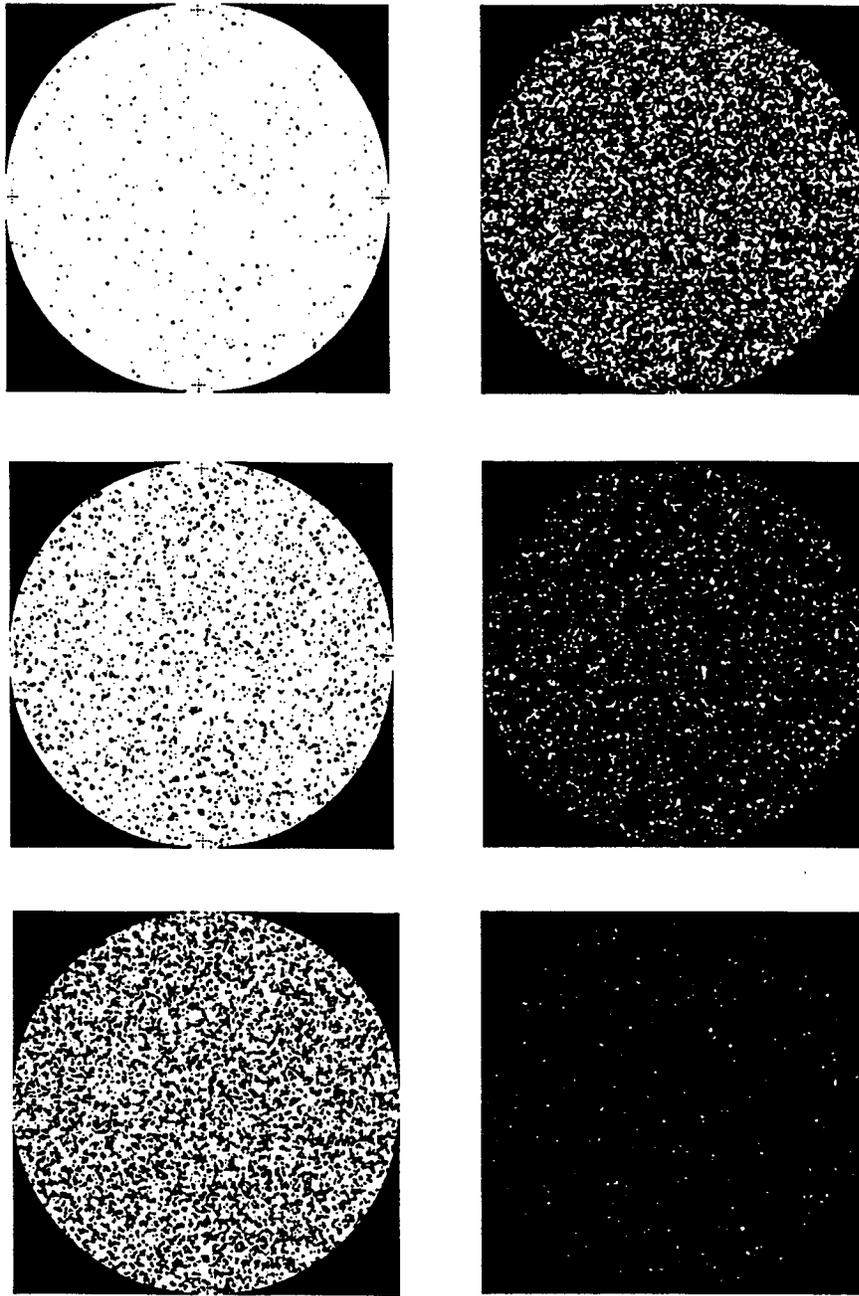
Figure 2: The six templates used to generate the random surface used in these experiments. Each circle has a 19.5 cm diameter to match the glass surface. Each template corresponds to one standard deviation of depth and each template was exposed to high velocity particles for the same amount of time. The numbering shows the order in which the templates were applied.

30

SIDE VIEW
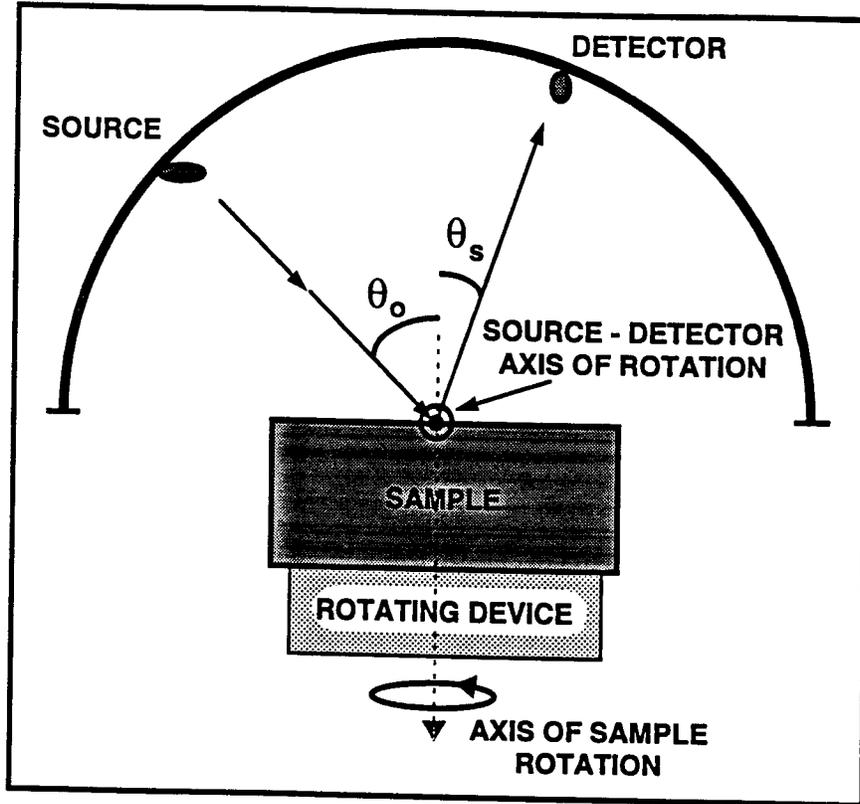
TOP VIEW
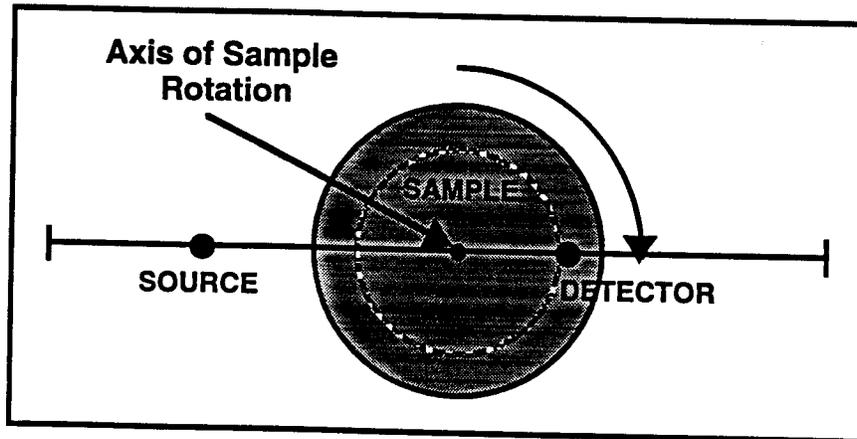
Figure 3: The geometry used to experimentally measure the scattering properties of a given random surface. The source is held stationary at one incident angle while the detector is stepped in a semi-circle about the random surface. This then gives one realization of that surface.
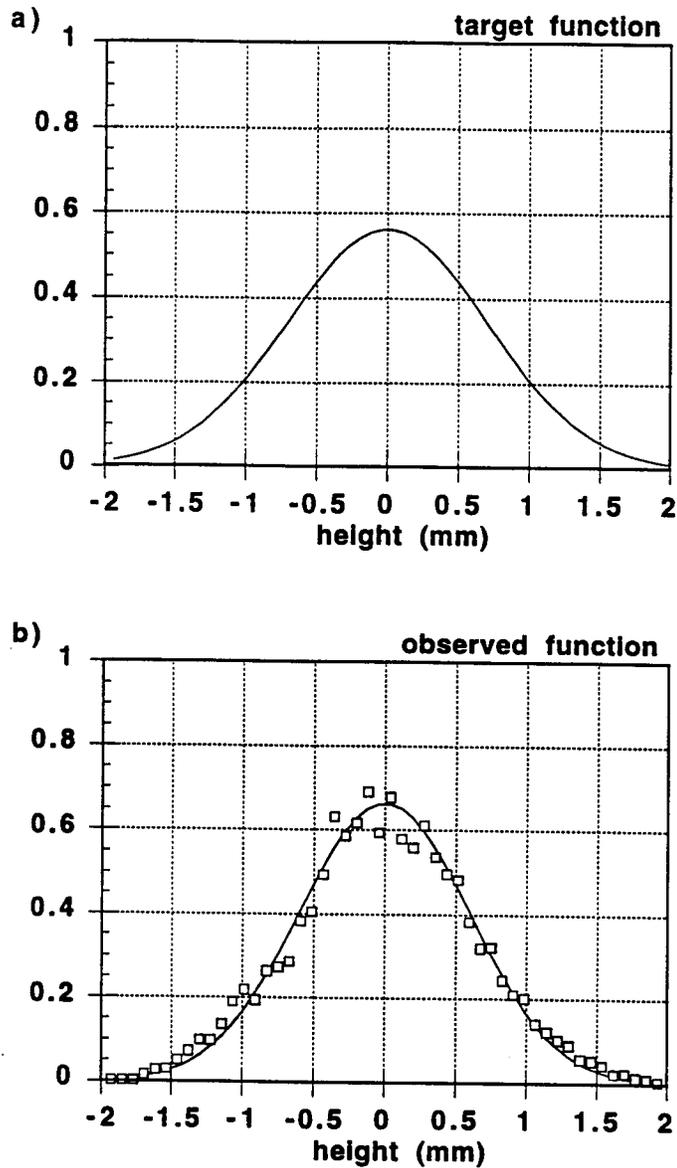
Figure 4: Histogram plotting surface height data. The target surface height distribution (a) is Gaussian with a standard deviation 1 mm. The surface height distribution (b) based on profilometer measurements (squares) of the glass surface is shown along with a best fitting Gaussian curve (solid line) which has a standard deviation of 0.6 mm. This histogram was plotted using 40000 surface profilometer measurements.
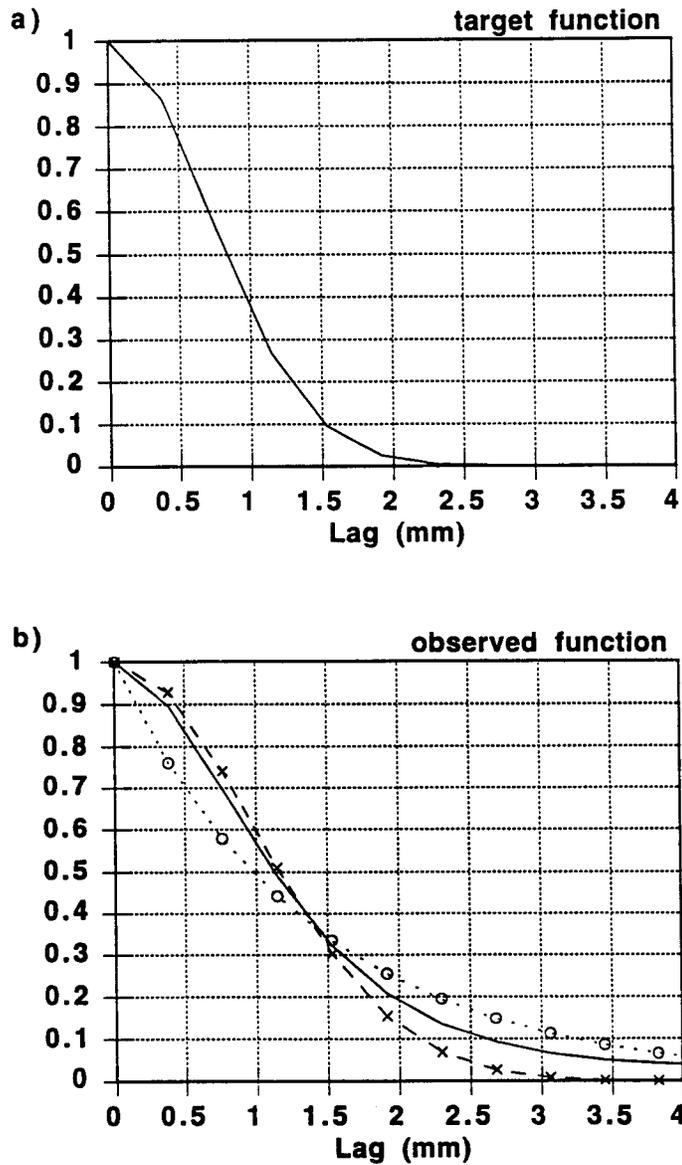
Figure 5: The interface autocorrelation function. The target autocorrelation function (a) is a Gaussian function with a correlation length e^{-1} of 1.0 mm. The actual autocorrelation function of the glass block (b) as calculated from profilometer measurements has a correlation length of 1.4 mm. The surface profilometer measurements (solid line) are compared with Gaussian (crosses) and exponential (circles) functions with the same correlation lengths of 1.4 mm.
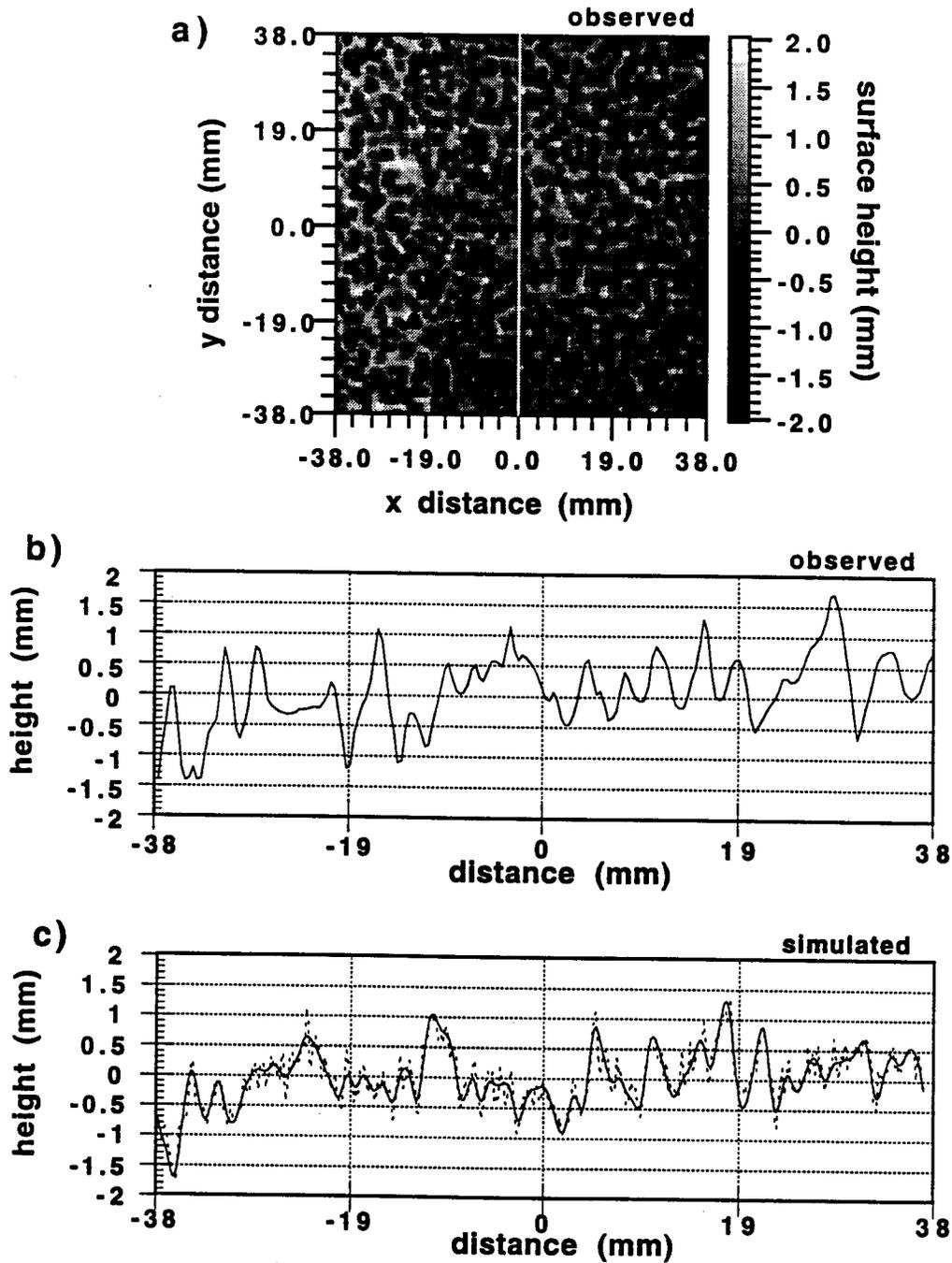
Figure 6: The surface height distribution based on profilometer measurements. (a) gives a grayscale plot of the surface, (b) gives a profile across the surface as marked in (a), and (c) shows a numerically generated surface with the statistics given in Figures 4 and 5. Both Gaussian (solid line) and exponential (dashed line) correlation functions are shown.

(a)

220.00   240.00   260.00   280.00

time (μs)

(b)

source wavelet

(c)

reflected wavelet
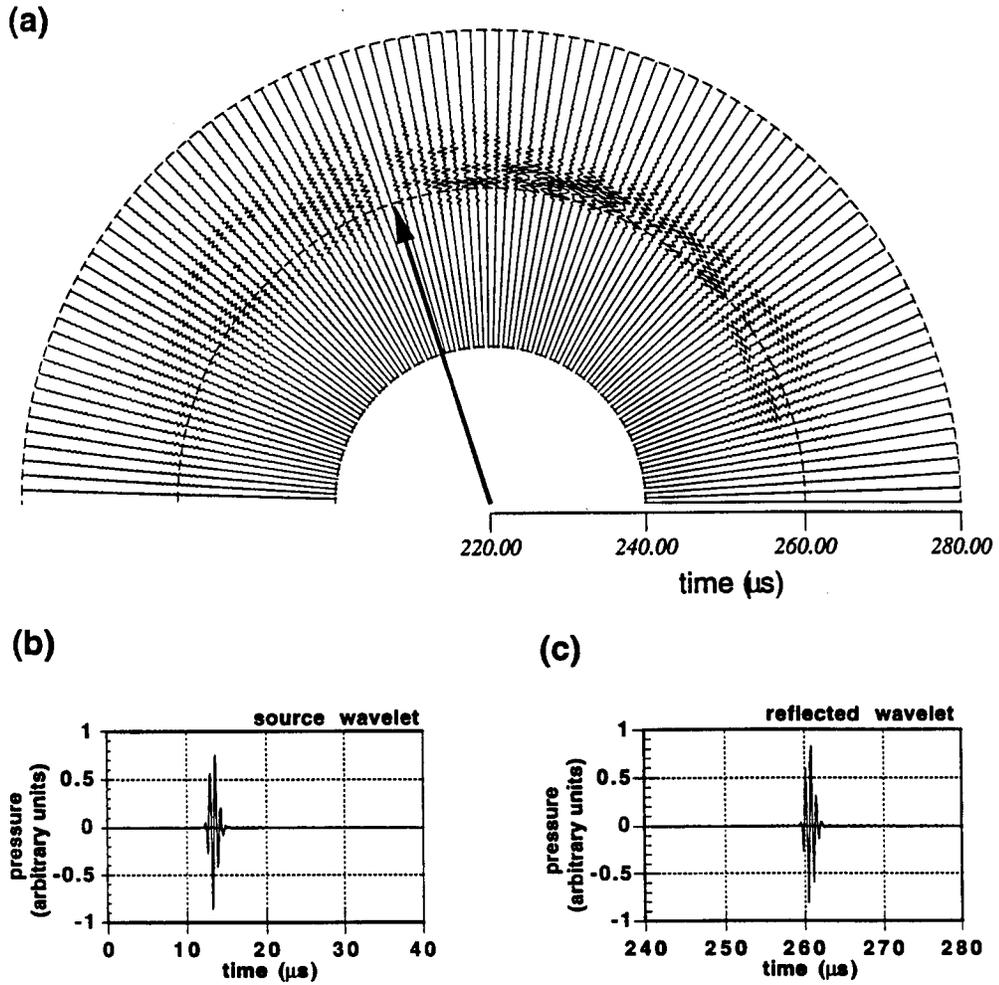
Figure 7: Experimental seismogram recorded over the glass model. (a) shows the seismic data recorded as a function of angle over the irregular glass surface with $\lambda = .71a$ given an acoustic beam incident at 20°. The arrow shows the retroreflective direction. The source wavelet (b) and the specular reflection (c) recorded over a plane interface are also shown. In the plane layer case the only observable energy is in the specular direction.

35
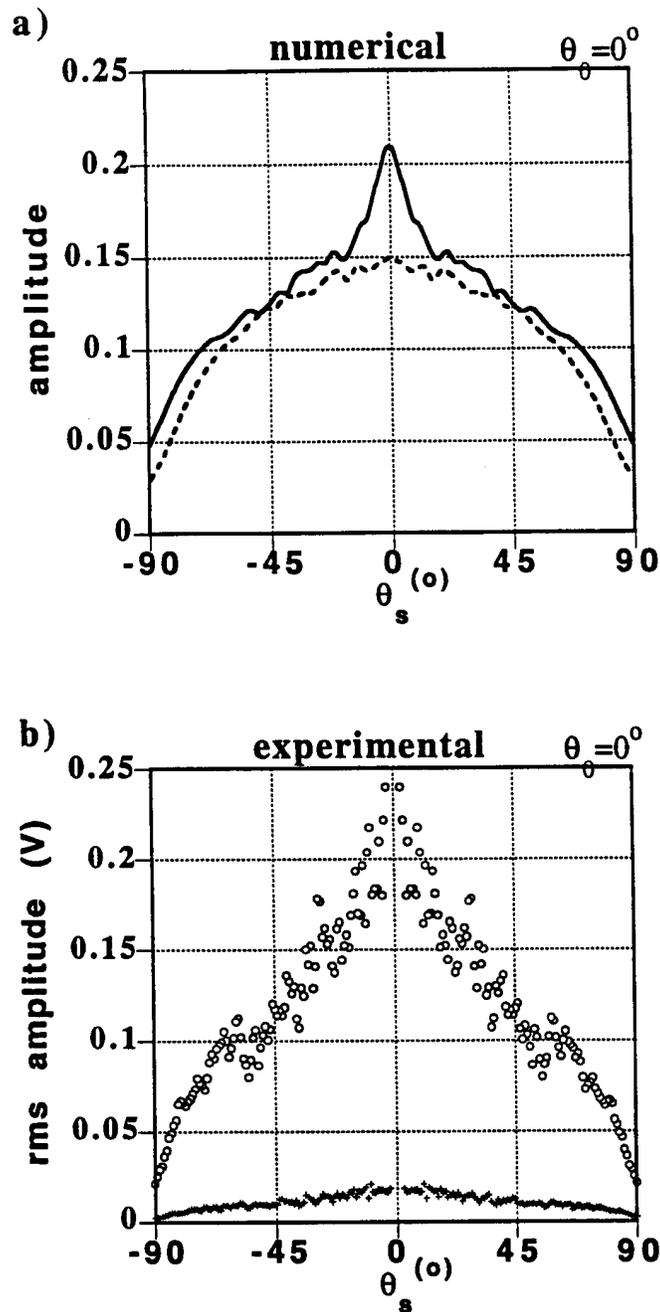
Figure 8: The 2-D mean reflection coefficient (a) calculated numerically over the Gaussian (solid line) and exponential (dashed line) surfaces given a normally incident source beam with $\lambda = .71a$. The 3-D reflection coefficient (b) recorded over the experimental interface (circles) and the standard deviation of the finite average (plus) are also shown. The experimental results correspond to 30 surface realizations.
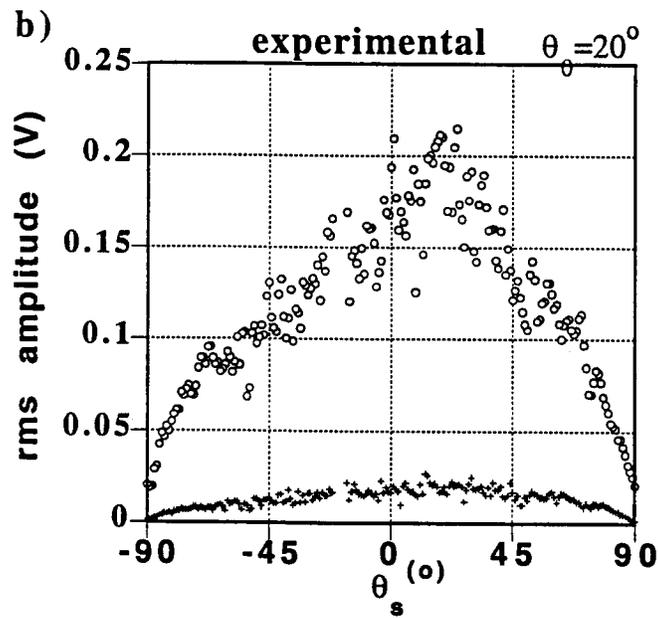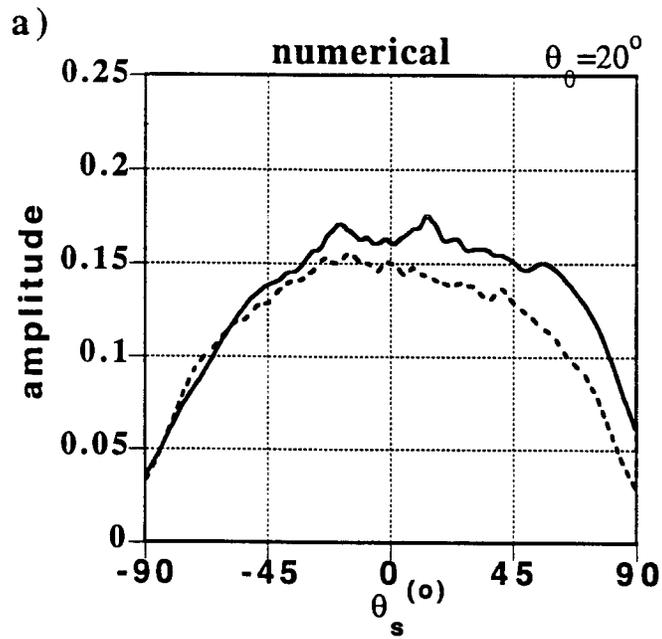
Figure 9: Similar to Figure 8, except the incident angle is now 20° and results correspond to 20 realizations.
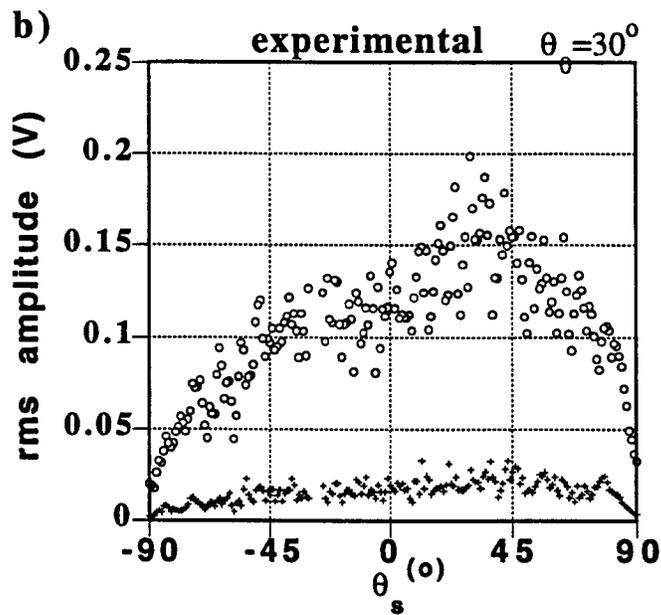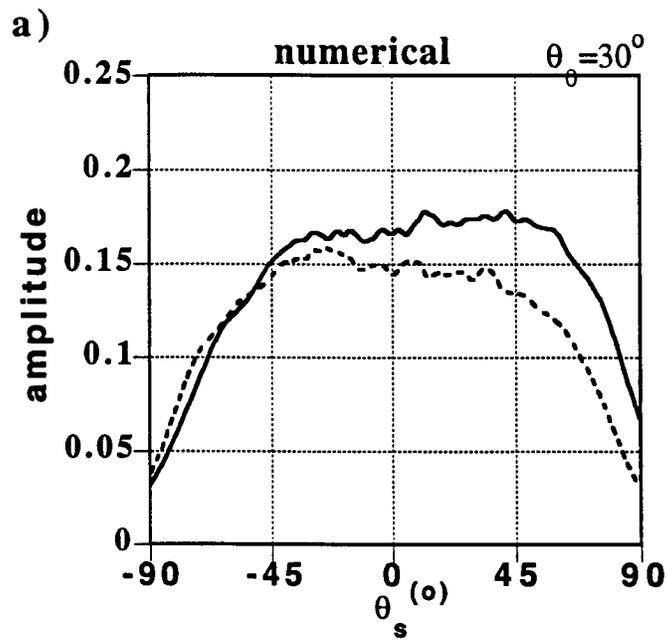
Figure 10: Similar to Figure 8, except the incident angle is now 30° and results correspond to 10 realizations.
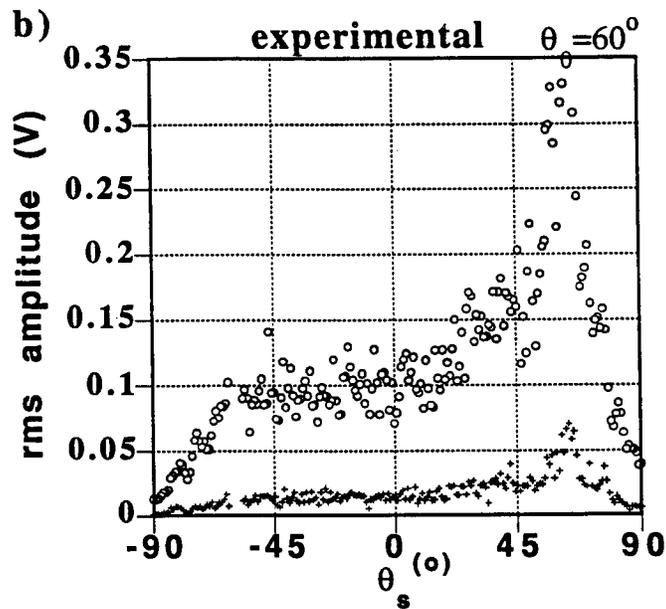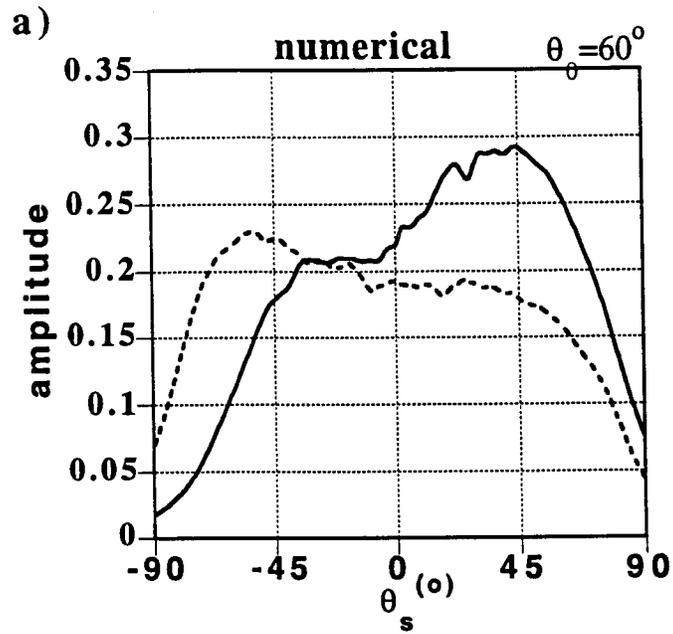
Figure 11: Similar to Figure 8, except the incident angle is now 60° and results correspond to 10 realizations.

(a)

(b)

(c)
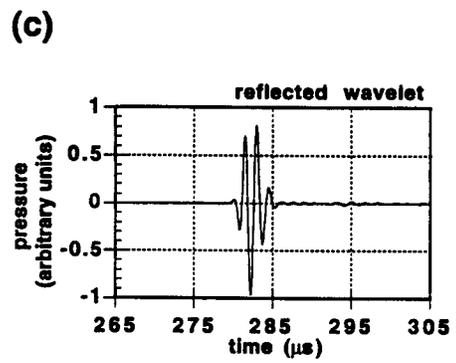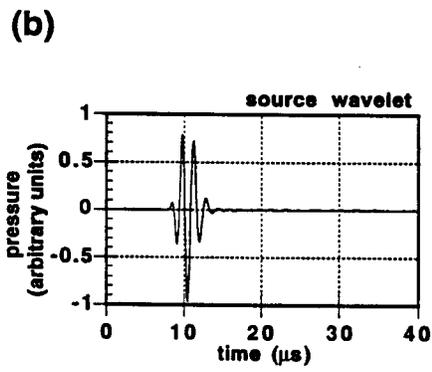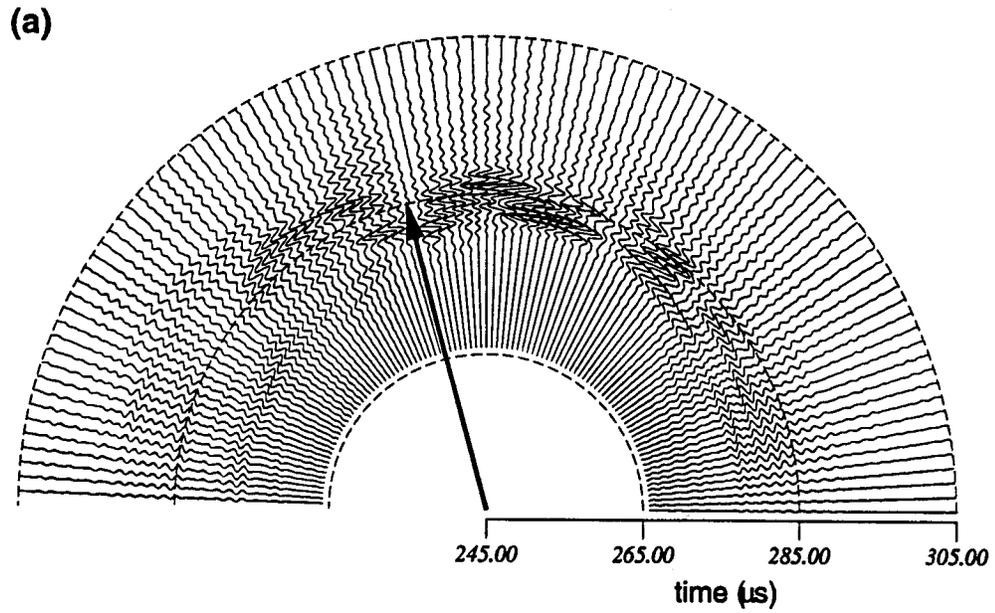
Figure 12: Similar to Figure 7, except $\lambda = 2.14a$.

40

a)

b)
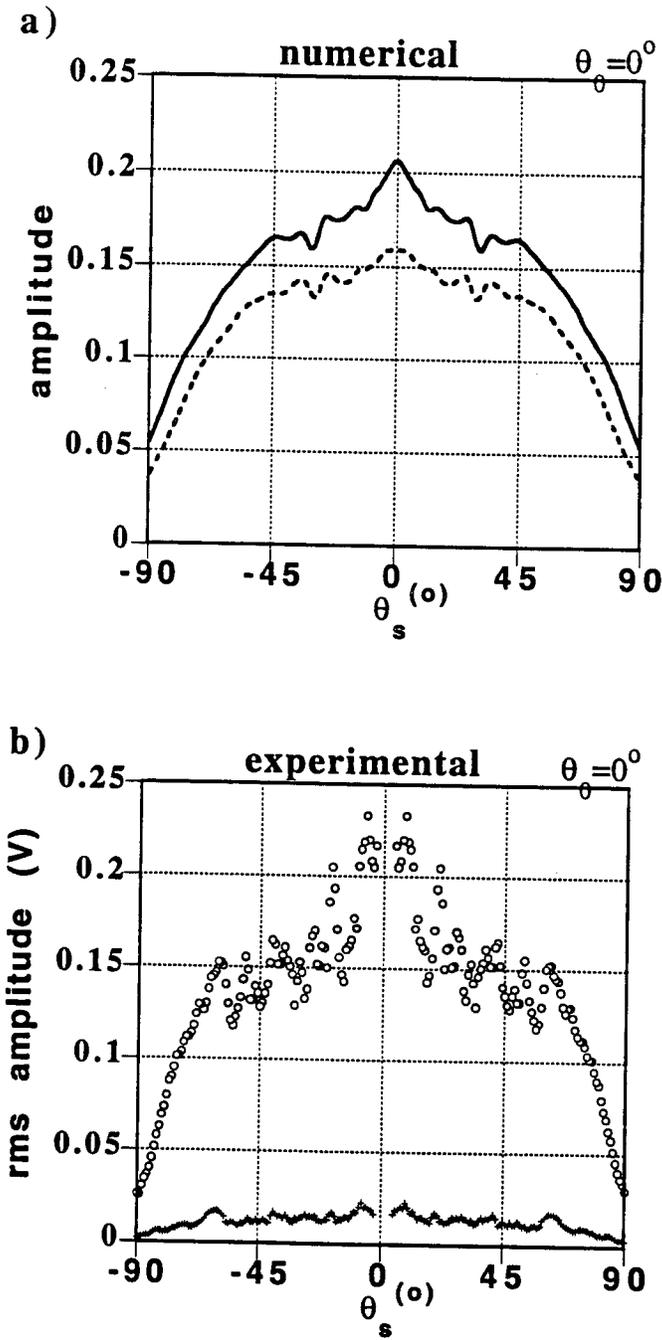
Figure 13: The 2-D reflection coefficient (a) calculated numerically over the Gaussian (solid line) and exponential (dashed line) surfaces given a normally incident source beam with $\lambda = 2.14a$. θ_s is the angle of forward (positive) and back (negative) scattering. The 3-D reflection coefficient (b) recorded over the experimental interface (circles) and the standard deviation of the finite average (plus) are also shown. The experimental results correspond to 30 surface realizations.

41
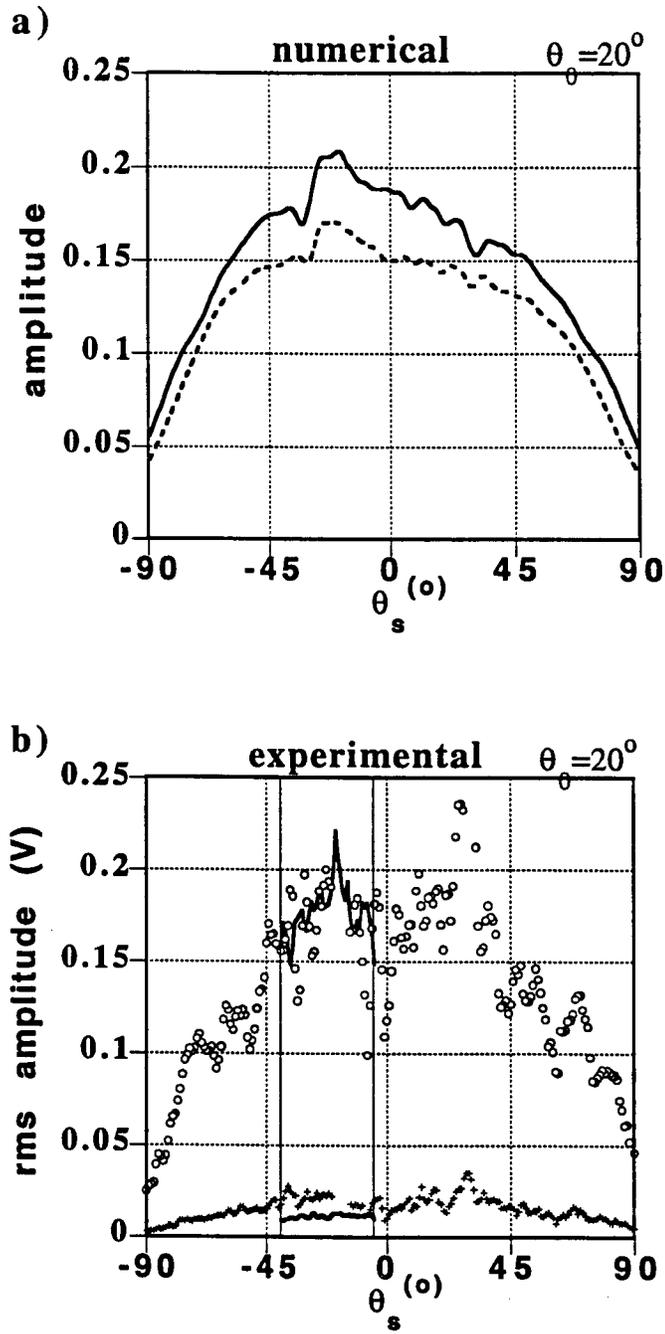
Figure 14: Similar to Figure 13, except the incident angle is now 20° and results correspond to 20 realizations.
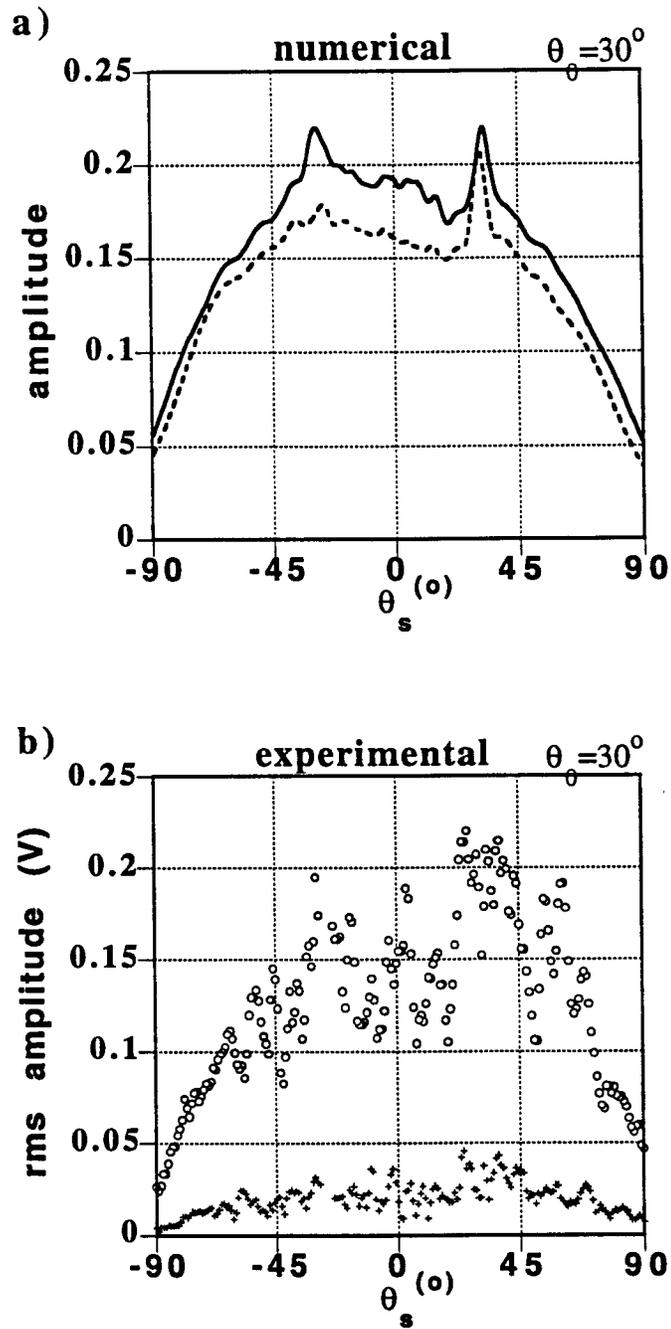
Figure 15: Similar to Figure 13, except the incident angle is now 30° and results correspond to 10 realizations.

a)

**numerical** $\theta_0 = 60^\circ$

b)

experimental $\theta_0 = 60^\circ$
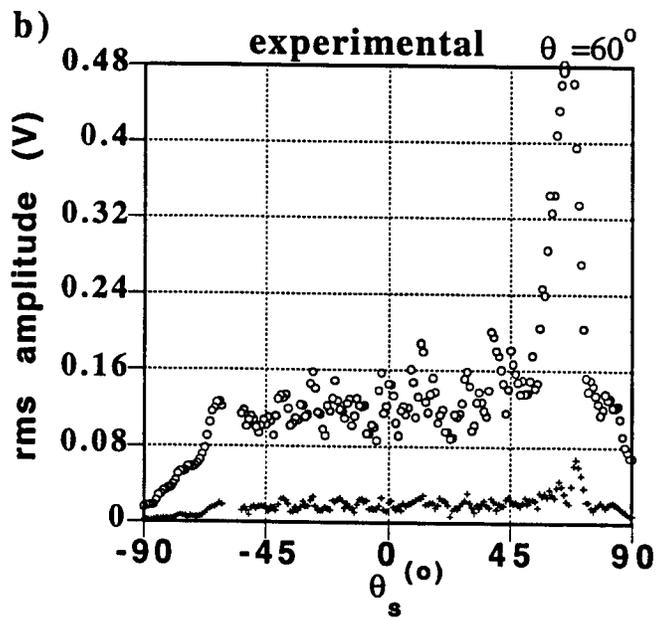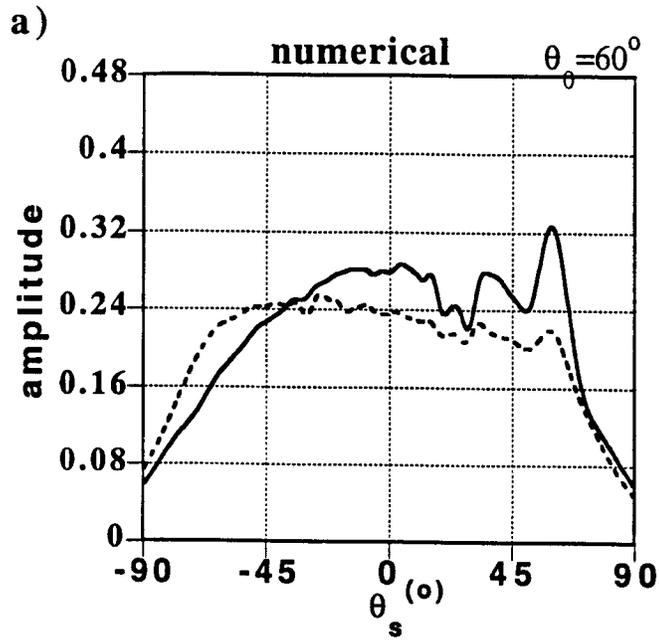
Figure 16: Similar to Figure 13, except the incident angle is now 60° and results correspond to 10 realizations.

44

CRUSTAL REFLECTIONS AND THE NATURE OF REGIONAL P CODA

Summary

F-K spectra for regional P coda are presented for events recorded at the Scandinavian NORESS, FINESA, and ARCESS arrays and the New England NYNEX array. The spectra are dominated by on-azimuth energy with apparent velocities between Pn (or faster) and Lg. Following this analysis, reflection coefficients calculated with an efficient boundary integral scheme are used to study the role irregular interfaces play in the creation of regional P coda. We find that observed crustal scattering in these regions is strikingly consistent with P-P and P-SV scattering from the 2-D irregular Moho and even more consistent with scattering from a 2-D irregular near surface interface.

Introduction

In recent years, understanding regional seismograms has attracted considerable interest, in part because of a desire to monitor small underground nuclear tests at regional distances. One of the characteristics of regional seismograms is coda, a train of waves without evident phases following the P and S arrivals. Previous work has shown that both regional P coda and S coda recorded in the crust are more complicated than the coda predicted for a plane layered crust. Dainty and Toksöz (1990) applied F-K analysis at Scandinavian arrays. They

found that at later times in the S coda, energy tends to arrive from all directions. This energy is consistent with the isotropic "standard model" of Aki and Chouet (1975), modified for the regional case by considering the scattering to be Lg to Lg (e.g., Herrmann, 1980). Teleseismic P coda appears to be similar in many respects to S coda (Dainty, 1990; Dainty and Harris, 1989; Dainty and Toksöz, 1990). Regional P coda, on the other hand, is more enigmatic and one model does not appear to explain the observations. The final model of regional P coda is likely a combination of various crustal scattering mechanisms.

Scattering due to irregular interfaces may give a better understanding of the incoherent, low amplitude arrivals which tend to complicate these seismograms. Recently, boundary integral techniques have been shown to be an effective tool in identifying which scattering mechanisms exist at a given interface. These efficient formulations have allowed the development of fast algorithms which can model statistical reflection coefficients over randomly irregular interfaces (Schultz and Toksöz, 1993; Schultz and Toksöz, 1994).

In this study, we illustrate how the reflection coefficients developed by Schultz and Toksöz (1994) can be used to gain insight into crustal scattering mechanisms. We first describe the general nature of regional P coda as recorded at Scandinavian (Mykkeltveit *et al.*, 1990) and New England (Dainty and Battis, 1989) arrays in terms of azimuth and phase velocity (angle of incidence) of energy. We characterize P coda using an F-K spectral approach. We then examine numerically derived reflection coefficients from Schultz and Toksöz (1994) to determine whether scattering from interface irregularities is consistent with the observed

F-K spectra.

The Nature of Regional P Coda

Regional P coda consists of a train of waves after Pn and Pg and before Sn and Lg at regional distances (100–2000 km). On the instruments used in this study, frequencies are in the range 1–20 Hz. Explanations for P coda include the scattering of P and S waves from distributed small heterogeneities in a similar manner to S coda, and multiple crustal reflections predicted by synthetic seismogram calculations in laterally homogeneous layered media. The results of Dainty and Toksöz (1990) show that P coda cannot be explained by the same model as S coda and a composite model which includes various forms of scattering may be required to explain P coda observed at arrays in Scandinavia. Such a composite model must consider the possibility of scattering from interface irregularities. Therefore, in this section, array data is studied in more detail to determine whether scattering from an irregular Moho and near surface layers is consistent with the observed P coda. We turn our attention to the analysis of regional P coda (100–2000 km) recorded at the Scandinavian NORESS, FINESA, and ARCESS arrays and the New England NYNEX array.

Figure 1 gives a synthetic vertical seismogram section for a plane layered crust recorded along an array of receivers at distances of 100 to 500 km from a vertical point force applied at a depth of .04 km (from Toksöz *et al.*, 1990). The model summarized in Table 1 is based on the NORESS crustal model of Sellevol and Warwick (1971) where $Q = Q_{P,S} f^{\varsigma}$, and serves to

Table 1: NORESS Crustal Model

Depth (km)	V_p (km/s)	V_s (km/s)	ρ (gm/cc)	Q_p	Q_s	ζ
0.0	5.2	3.2	2.6	50	25	0.5
3.0	6.0	3.5	2.7	200	100	0.8
17.0	6.51	3.8	2.9	1000	500	0.0
38.0	8.05	4.67	3.3	2000	1000	0.0

illustrate the effects discussed. Referring to Figure 1 the synthetic results show that a plane layered crust results in P coda energy which will arrive on azimuth, with the predominant energy showing phase velocities between Pg and Pn. P-SV bounces are included but they have high, Pg-Pn, phase velocities. This behavior is caused by rays with multiple bounce points in the crust, mainly on the Moho and the free surface where at least one leg is P. At larger offsets the energy in P coda converges to a Pg phase velocity. Energy is not expected at velocities lower than Pg or higher than Pn. Also, the P coda energy in this plane layer model is coherent with arrival groups that may be correlated across traces. This coherence is not observed in real seismograms. The phenomenon of multiple post-critical crustal bounces potentially distinguishes regional P coda from teleseismic P coda, where crustal reflections will be precritical and of low energy.

F-K Analysis

F-K analysis is used to find the velocity and azimuth of the dominant and secondary energy observed in the P coda at the four arrays: NORESS, ARCESS, (Mykkeltveit *et al.*, 1990)

Table 2: Event parameters and measured azimuths and velocities from frequency-wavenumber analysis

Date yyddd	OT(UTC)[a]	Type[b]	Distance[a] (km)	Analysis Freq (Hz)	P Az	1st Peak		2nd Peak		3rd Peak	
						Az	V (km/s)	Az	V (km/s)	Az	V (km/s)
ARCESS											
87307	22:35:13	?	420	3.8	244.0°	233.0°	8.0	230.5°	3.8		
87350	11:48:54	M	370	2.4	114.0°	107.0°	8.5				
88116	20:09:05	E	1160	2.2	294.5°	247.0°	4.5				
88128	22:49:52	N	1030	2.0	64.5°	43.0°	5.8	50.0°	3.45		
90047	12:38:16	M	420	4.0	122.0°	123.0°	7.9	120.0°	3.45		
90054	09:31:24	M	430	4.0	122.0°	120.0°	6.2	113.5°	4.2		
FINESA											
85319	13:53:37	M	240	4.0	97.0°	106.0°	4.1				
85354	12:38:53	M	230	4.0	184.0°	209.0°	7.25	218.0°	3.9		
85359	14:18:01	M	220	4.0	109.0°	90.5°	7.1				
85361	11:06:26	M	340	4.0	99.0°	93.5°	5.2				
85361	12:16:08	M	300	4.0	140.5°	154.0°	6.0	149.0°	3.7		
NORESS											
85058	12:58:31	M	320	2.4	243.0°	226.0°	6.0				
85300	04:36:09	E	360	6.5	280.0°	284.0°	7.6				
85331	04:53:14	E	340	5.0	253.0°	251.0°	7.5	263.5°	3.9		
86038	10:59:50	M	1070	3.0	57.0°	58.0°	8.5	78.5°	4.1		
86045	14:13:34	M	390	3.0	229.0°	246.0°	7.8	212.5°	6.25	224.5°	4.0
NYNEX											
88261	09:00:00	R	165	15.0	91.0°	144.0°	15.7	40.0°	6.7		
88261	09:08:00	R	198	11.0	264.0°	278.0°	4.6				
88261	11:04:00	R	189	12.0	82.0°	74.0°	10.5				
88268	09:04:00	R	159	7.0	263.0°	353.0°	18.1				
88274	11:04:00	R	240	8.0	258.0°	396.0°	4.7				

[a]Calculated from S-P time, or taken from Helsinki Bulletin, or taken from shot table.
[b]E= Earthquake, M = Mine Blast, N = Presumed Nuclear Test, R = Refraction Shot, ? = Unknown

FINESA, (Uski, 1990) and NYNEX (Battis, 1990). A combined total of 21 events were studied consisting of a combination of mine blasts, nuclear blasts, refraction shots (NYNEX) and earthquakes (Table 2). Figure 1 gives an example of the processing and analysis, where the seismogram corresponds to the vertical displacement recorded at the center station of NORESS%. The event was a quarry blast at Titania Quarry, which is 393 km away from the array with an azimuth of 228°. The algorithm used for F-K analysis is that described in Dainty and Toksöz (1990). The seismogram is filtered in a narrow pass-band, $+/-10\%$, around a central frequency of 3 Hz and the frequency–wavenumber spectrum is calculated

using the Maximum Likelihood Method (MLM) (Capon, 1969). A window of 20 sec duration was used for NORESS, ARCESS, and FINESA data, 10 sec for NYNEX data; the windows were picked by hand. While the analysis method allows overlapping windows, this was not used in this study. Frequencies were chosen to be within the range that had significant power in the data, usually the peak frequency. The MLM method gives the resolution in wavenumber needed for this study; a narrow band was used because our experience with broadband MLM is that it is very computer intensive and narrow band MLM was used with success by Dainty and Toksöz (1990). All velocities and azimuths reported here were determined by this method.

The results from the F-K analysis showed peaks at close to the source azimuth. This encouraged us to use semblance analysis to determine the apparent velocity of P coda energy as a function of time along the source azimuth (228° in Figure 2) (Dainty and Schultz, 1993). The semblance S at slowness s was calculated by the standard formula (Kanasewich, 1975, p. 252)

$$S(s) = \frac{\sigma_{i=n}^{m} b_i^2}{M \sigma_{i=n}^{m} \sigma_{j=1}^{M} f_{ij}^2}$$

where f_{ij} are the seismogram values at array station j and time index i, b_i are the values of the beam at slowness s (and the source azimuth) at time index i, M is the total number of array stations, and the summation over i represents the time window over which the semblance is calculated. This quantity was calculated in 2 sec windows overlapped by 1 sec and a slowness range of 0.0 to 0.1 sec/km at the source azimuth. The resulting grid of values

was contoured to show where coherent energy was arriving in time (cf. Figure 2). Semblance has a range of zero to one and is a very sensitive indicator of the presence of coherent energy; in Figure 2 light areas in the semblance plot have a semblance of 0.4 and greater. However, it must be noted that velocities correponding to peaks on the semblance plot shown in Figure 2 will only be correct if the energy is arriving at exactly the azimuth used to construct the beams (228°). For this reason velocities were not picked from the semblance plots.

F-K analysis of P coda energy assists in the elucidation of crustal scattering mechanisms. This preliminary analysis involved picking by hand the phase velocities and azimuthal deviations of energy peaks in the F-K spectra. The peaks were chosen based on several criteria. Generally, one or two peaks were picked on a plot and for one event (Figure 2) three peaks were picked. The peaks selected were the highest peaks, at least one contour level above the surrounding noise with phase velocities faster than 2 km/s. The largest peak was chosen as a primary peak and the remaining peak(s) were labeled as secondary. No secondary peak was more than 6 db below the primary, and all but one were within 3db. Figure 3 gives the histograms for the phase velocity and azimuthal distribution of the data and includes both primary and secondary peaks. The peaks cluster around the source azimuth (most peaks within 20°). This contrasts with the S coda where the energy is spread over all azimuths. This F-K analysis shows energy arriving between Pg and Pn phase velocities as predicted by the plane layered geometry. Peak energy is observed at Pn phase velocity and greater. Not predicted by the plane layer model, a large amount of energy arrives with slower phase

velocities, between Lg and Pg, with primary peak energy arriving at Sn. A peak number of secondary arrivals are also observed with approximate Lg velocity. Each of these slower arrivals suggests that P waves are converted during some leg of the path into post critical-shear energy which then becomes favored for lateral propagation. The semblance analysis generally confirms the F-K observations as Pn and Pg energy tends to arrive early in the P coda while Lg energy tends to arrive late. This time delay is expected with conversion to shear along at least one leg of the path. In general this F-K analysis shows that P coda energy is usually dominated by a few peaks which arrive with different phase velocities of approximately the same azimuth rather than a single phase velocity with substantially different azimuths, characteristic of S coda.

Although volume scattering appears to explain the scattering responsible for S coda, the wide range of phases and the absence of diffuse scattering over a wide range of azimuths in P coda suggests a different scattering mechanism. Many mechanisms may be responsible for the observation of slower phases in P coda at these arrays. Sanchez-Sesma and Campillo (1991), among others, have shown theoretically that even simple topographic features near an array can cause great variability in recorded amplitudes as a function of frequency, incident angle, and receiver location with respect to the topography and observations confirm this (Bannister *et al.*, 1990, Gupta *et al.*, 1990). Heterogeneities near the receiver array can also play havoc with any F-K interpretation as near field interference spreads and distorts coherent arrivals on seismograms. Another mechanism which also must be considered is

wave conversion at irregular crustal interfaces such as the Moho and shallow near surface interfaces.

We assume that F-K analysis emphasizes energy consisting of plane wave components, and thus accentuates waves scattered more than a few wavelengths from the array. We now show that the energy scattered at irregular crustal boundaries is consistent with the energy observed at the NORESS, FINESA, ARCESS, and NYNEX arrays.

The Role of an Irregular Moho

We will analyze the F-K results in terms of scattering of plane waves incident upon an irregular interface, taken here to be the Moho. The comparison between reflection coefficients and F-K spectra is based on the relation $v_{app} = v_{true}/sin\theta$, where v_{app} is the apparent (phase) velocity measured across the array, v_{true} is the velocity of the surface or crustal material, and θ is the angle of propagation to the vertical. We utilize the Somigliana approach of Schultz and Toksöz (1993, 1994) to calculate the effects of scattering. This approach models all waves scattered at an interface, including all converted, multiple scattered, and interface waves generated along the interface. The scattered energy at any point along the interface is presented in the form of amplitude reflection coefficients, showing on average the amplitude distribution for waves propagating away from the irregular interface.

Characterizing the interface with specific Gaussian statistics the interface roughness can be expressed in terms of the standard deviation of interface height, δ, and an autocorrelation

length, a, which represents approximately the average distance between adjacent peaks and valleys along the interface. The average *rms* slope of the interface can be expressed as

$$\phi = tan^{-1}(\frac{\sqrt{2}\delta}{a}).$$ (1)

We consider the numerical solutions for two specific crustal boundaries which may be highly irregular. The first case is an irregular Moho where we assume that the lower crust has a P wave velocity of 6700 m/s, an SV velocity of 3900 m/s, and a density of 3.0. The mantle is given a P wave velocity of 8200 m/s, an SV wave velocity of 4700 m/s, and a density of 3.3. In these cases we have selected rather extreme velocity contrasts so that various scattering phenomena may be accentuated. The second case is a shallow near surface soil-basement interface where the overlying sediment is given a P wave velocity of 2000 m/s, an SV wave velocity of 1200 m/s, and a density of 2.0 which represents an unconsolidated or semiconsolidated sediment. The basement rock is given a P wave velocity of 6400 m/s, an SV wave velocity of 3200 m/s, and a density of 2.7. Figures 5 and 6 show the statistical reflection coefficients for a P wave incident on a Moho with both a 10° *rms* slope and a more irregular 30° *rms* slope, respectively. These reflection coefficients correspond to the case $a \approx \lambda$ presented in Schultz and Toksöz (1994), where both reflected P and converted S amplitudes are plotted at specific incident angles, ranging from normal incidence ($\theta_0 = 0^o$) to near grazing angles ($\theta_0 = 60^o$). In each case the total displacement amplitude is plotted, including specular contributions. Note also that in each figure, negative scattering angles, θ_s, corresponds to backscattering.

A simplified crustal model, where a constant velocity crust is bounded by a plane free surface and an irregular Moho as shown in Figure 4a, can help elucidate the generation of P coda. In the case shown, an incident P wave encounters an irregular Moho, generating both P and converted S energy over a broad range of directions, including the specular direction. Referring to the reflection coefficients for an irregular Moho, shown in Figures 5 and 6, it is clear that in the 3–4 Hz frequency range characteristic of the Scandinavian events, Moho roughness of 100–500 m over 1–2 km range can explain the observed scattering trends. At the higher frequencies, typical of the NYNEX data, 30–200 m variations over 300–600 m would be appropriate. P-to-P scattering at most incident angles favors a lobe of scattering with the peak amount of energy scattered at Pn phase velocity (critical angle) and a full spectrum of energy scattered between Pn and Pg phase velocities (post-critical angles) given most incident angles. These waves add to energy arriving in the specular direction, contributing to the wavefield with Pn and Pg phase velocity. At all incident angles, P-to-S reflection coefficients show a peak conversion to phase velocities faster than Sn. At incident angles greater than 40°, energy is converted to post-critical shear waves. Since the peak S energy, $V_a \geq Sn$, leaks out of the crust, the most efficient modes of propagation are waves travelling with Sn phase velocity. Lg velocities are also favored, although less energy is converted to these waves. This distribution of energy corresponds well to the observed data where Sn and Lg velocities are seen. Moving to the more irregular case of a 30° rms slope, shown in Figure 6, this post-critical scattering becomes more pronounced, demonstrating that larger

interface roughness can give even greater preference to the propagation of Sn and Lg phase velocities in the crust.

It may be remarked that it is not neccessary for the Moho to be rough at all places; patches of roughness would be sufficient. Reflection profiling of the continental Moho (e.g., Braile and Chang, 1986) suggest this could be the case. The semblance analysis (Figure 2) shows bursts of coherent energy within the P coda; these bursts could be associated with specific areas of roughness.

The Role of Near-Surface Intracrustal Layers

Can rough intracrustal interfaces be partially responsible for peak Sn and Lg phase velocities observed in the F-K analysis of P coda? Figure 4b gives an example of a simplified crustal geometry which can contribute post-critical shear energy to the lower crust. In this case, an upward propagating P wave, travelling in a constant velocity lower crust, scatters as it encounters a highly irregular soil-basement interface. Incident energy is converted into post-critical shear energy which is then favored for lateral propagation in the crust. Looking at the statistical reflection coefficients for an irregular soil-basement interface, it is apparent that such near surface scattering may actually give a far stronger contribution to post-critical shear energy than the Moho. Figure 7 shows reflection coefficients for a P wave incident, from the lower crust, on a soil-basement interface with an *rms* slope of 30°. It is clear that this interface can scatter the same order of energy as the Moho into phases which travel with Sn

and Lg phase velocities, and this conversion can now occur not only at grazing angles, but also at most other incident angles, generating additional post-critical energy in the lower crust. While the soil-basement reflection case is shown for illustration here, we generally expect strongly irregular interfaces present in the near surface intracrustal region (including the free surface) to strongly influence the production of scattered energy, especially at lower phase velocities.

Just as the scattering from the bottom of a highly irregular near surface interface can create large amplitude, post-critical energy which remains trapped in the crust, the scattering of P wave energy incident from the top of a near surface interface can generate large amplitude energy which is favored for lateral propagation over short distances in the shallower crustal layers, as shown in Figure 4c. Figure 7 shows the reflection coefficients presented for the soil-basement interface, given a P wave incident from the soil layer. These reflection coefficients show that large amounts of scattered P and converted SV energy is scattered to post-critical angles. This energy would likely be observable only at nearby stations, since waves tend to be highly attenuated in these shallower layers.

Additional Remarks on Interface Scattering

The above discussion assumes 2-D interface structure. The results for the less irregular Moho ($\phi = 10^o$) may be compared with the 3-D single-scattering perturbation results of Prange (1989). There is a strong similarity in the scattering results over interfaces with

similar Gaussian statistics. Post-critical peaks and nulls match well in both scattering angle and relative amplitudes, strengthening the assertion that 2-D scattering can give us insight into the mechanisms of 3-D scattering. It should be noted that the reflection coefficients presented by Prange (1989) do not include specular contributions.

Discussion and Conclusions

An analysis of events recorded at the NORESS, FINESA, ARCESS, and NYNEX arrays using F-K spectra showed that backazimuths of P coda energy cluster around the P backazimuth with a spread of about +/-15°. The F-K spectra contained tight peaks which do not spread over large azimuths. This contrasts to the behavior of S coda, and indicates that a model of scattering from a distributed homogeneity is not adequate, at least for the coherent portion of the coda. The velocities measured fall into three main groups: a high velocity group (> 7 km/s), a Pg velocity (6 km/s) group, and a low velocity (< 5 km/s) group. The high velocity group fits the multiple crustal reflection model, and is also favored by P-P scattering from a rough interface. The other velocity groups may be explained in term of scattered, nonspecular reflections from a rough interface. Scattering from an irregular Moho and irregular near surface intracrustal interfaces are both shown to be consistent with these observations. It should be noted that the observations reported here were all taken on stable continental crust, and all conclusions apply to this situation. The more irregular the Moho discontinuity or the shallow intracrustal interface, the more easily energy is converted to the

phase velocities observed at the arrays. In addition, a near surface interface in the shallow crust can also efficiently generate scattered energy which is favored for lateral propagation in the upper crustal layers. The effects of large attenuation in shallower crustal layers may decrease the importance of these waves. This preliminary study indicates that a composite model for scattering within the crust must consider the possibility of scattering from interface irregularities.

Acknowledgements

References

Aki, K., and Chouet, B., 1975, Origin of coda waves: source, attenuation, and scattering effects, *J. Geophys. Res., 80*, 3322–3342.

Battis, J.C., 1990, Data report for the 1988 Ontario-New York-New England seismic refraction experiment: small-aperture array, *Geophysics Laboratory Scientific Rept. GL-TR-90-0178*, Hanscom AFB MA 01731-5000.

Bannister, S.C., Husebye, E.S., and Ruud, B.O., 1990, Teleseismic P coda analyzed by three-component and array techniques: deterministic location of topographic P-to-Rg scattering near the NORESS array, *Bull. Seism. Soc. Am., 80*, 1969–1986.

Braile, L.W., and Chiang, C.S., 1986, The continental Mohorovičić discontinuity: results from near-vertical and wide-angle reflection studies, in *Reflection Seismology: a Global Perspective*, Barazangi and Brown (eds.), Geodynamics Series v. 13, American Geophysical Union, pp. 257–272.

Capon, J, 1969, High-resolution frequency-wavenumber spectrum analysis, *Proc. IEEE, 57*, 1408–1418.

Dainty, A.M., 1990, Studies of coda using array and three-component processing, *PAGEOPH, 132*, 221–244.

Dainty, A.M., and Battis, J.C., 1989, Variation in apparent azimuth of arrivals at a small aperture array in New England, *EOS, Spring Mtg. Suppl.*, p. 400.

Dainty, A.M., and D.B. Harris, 1989, Phase velocity estimation of diffusely scattered waves,

Bull. Seis. Soc. Am., *79*, 1231–1250.

Dainty, A.M., and Schultz, 1993, Reflections and the nature of P coda, *EOS, Spring Mtg. Suppl.,* p. 211.

Dainty, A.M., and Toksöz, M.N., 1990, Array analysis of seismic scattering, *Bull. Seism. Soc. Am.,* *80*, 2242–2260.

Gupta, I.N., Lynnes, C.S., and Wagner, R.A., 1990, Broadband F-K analysis of array data to identify sources of local scattering, *Geophys. Res. Let.,* *17*, 183–186.

Herrmann, R.B., 1980, Q estimates using the coda of local earthquakes, *Bull. Seism. Soc. Am.,* *70,,* 447–468.

Kanasewich, E.R., 1975, *Time Sequence Analysis in Geophysics*, Univ. of Alberta Press, 364 pp.

Mykkeltveit, S., Ringdal, F., Kværna, T., and Alewine, R.W.,1990, Application of regional arrays in seismic verification research, *Bull. Seism. Soc. Am.,* *80*, 1777–1800.

Sanchez-Sesma, F.J. and Campillo, M., 1991, Diffraction of P, SV, and Rayleigh waves by topographical features: A boundary integral formulation, *Bull. Seism. Soc. Am.,* *81*, 2234–2253.

Schultz, C.A. and Toksöz, M.N., 1994, Enhanced backscattering of seismic waves from a highly irregular interface: P-SV case, *Geophys. J. Int.,* in press.

Schultz, C. and Toksöz, M.N., 1993, Enhanced backscattering of seismic waves from a highly irregular interface: SH case, *Geophys. J. Int.,* *114*, 91–102.

Sellevoll, M. and Warrick, R., 1971, A refraction study of the crustal structure in Southern Norway, *Bull. Seism. Soc. Am., 61*, 457–471.

Toksöz, M.N., Cheng, N., Dainty, A.M., and Mandal, B., 1990, Regional seismograms: attenuation, scattering and anisotropy, *Proc. 12th Ann. DARPA/GL Seis. Res. Symp.*, 166–176.

Uski, M., 1990, Event detection and location performance of the Finesa array in Finnland, *Bull. Seism. Soc. Am., 80*, 1818–1832.

SYN. RECORD SECT., SMOOTH INTERFACES
(TOKSÖZ ET AL., 1990)
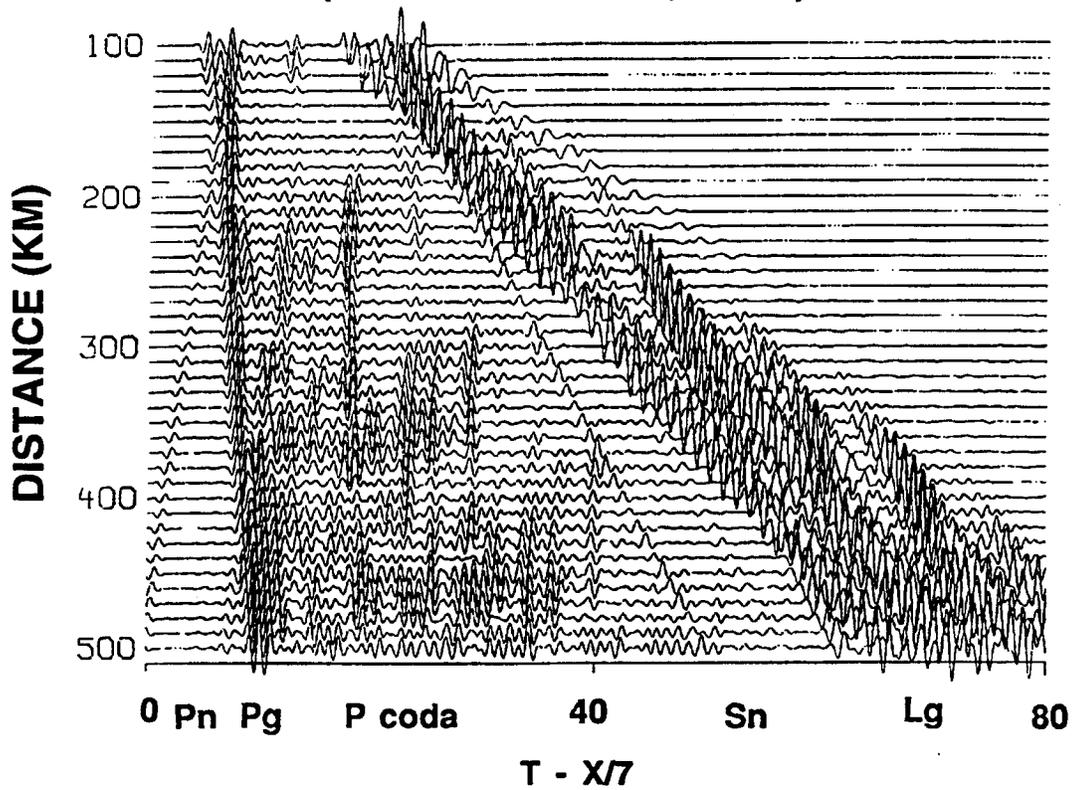
Figure 1: A synthetic seismogram calculated with reflectivity over a simply layered crust following a velocity model for NORESS, which is shown in the text. The various phases are labeled.

63
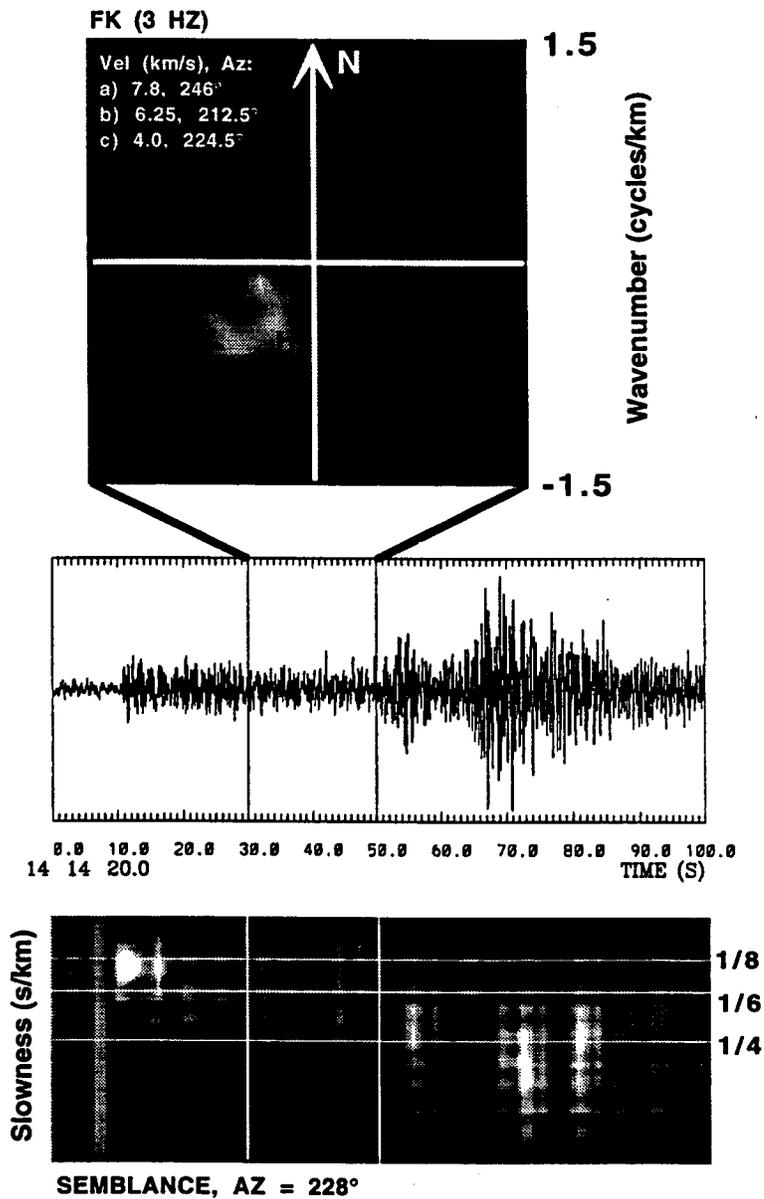
Figure 2: The frequency-wavenumber spectrum for the P coda window shown. The position, phase velocity, and azimuth of the primary peaks are given. Also shown is the semblance analysis for this time window.
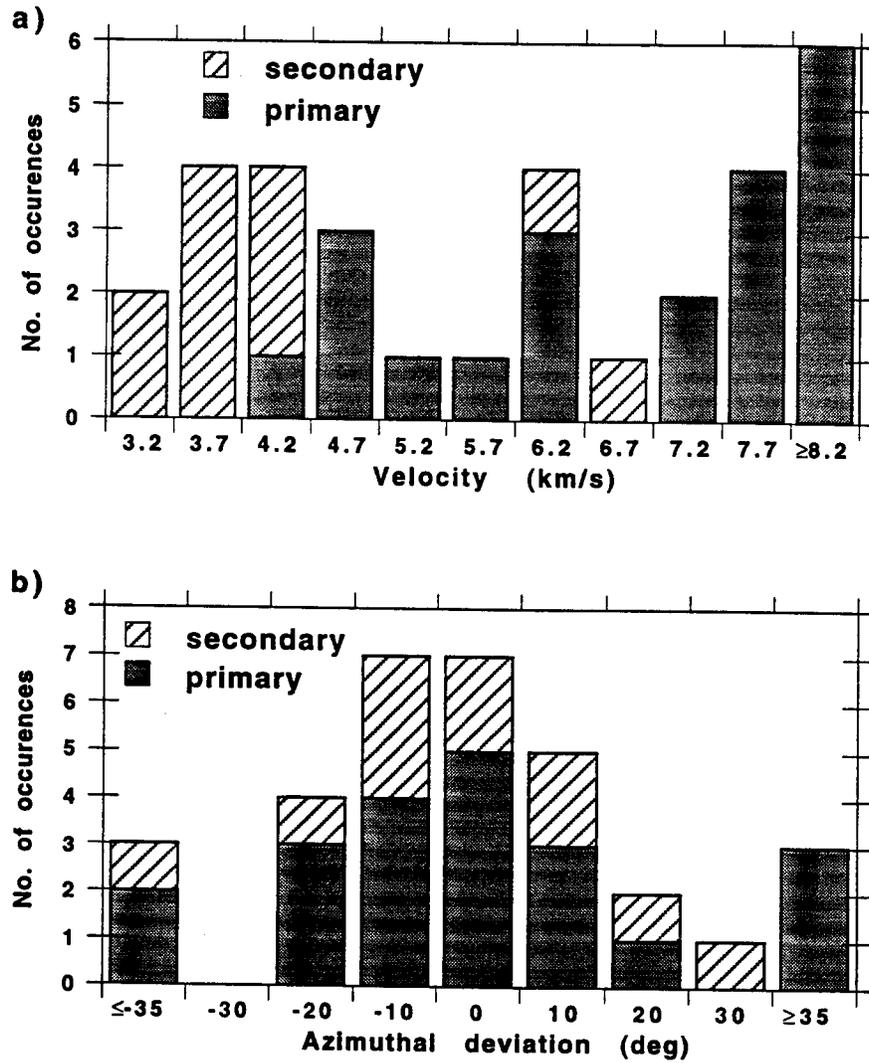
Figure 3: Histograms giving (a) the distribution of phase velocities and the (b) azimuthal deviation of events as measured by hand from the F-K plots for the data analyzed at NORESS, FINESA, and ARCESS.
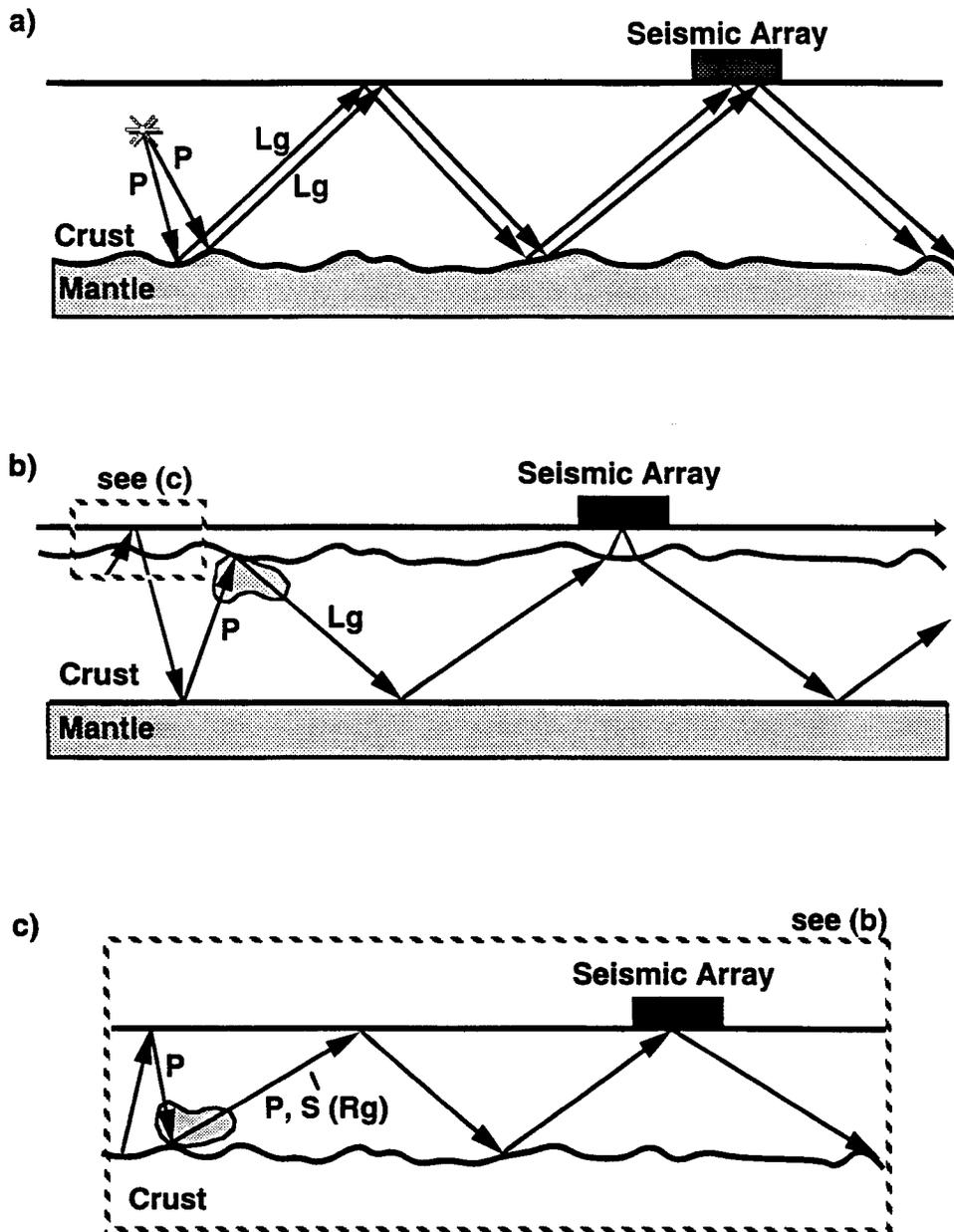
Figure 4: A simplified diagram showing (a) an irregular Moho and (b) a near surface, soil-basement interface generating energy which then travels with Sn-Lg phase velocities in P coda. Also shown is (c) a shallow near surface layer contributing to P and S energy which becomes trapped within a shallow surface layer, potentially complicating Rg energy recorded at a nearby seismic array. The grayscale regions represent the corresponding mean reflection coefficient for the given boundary.
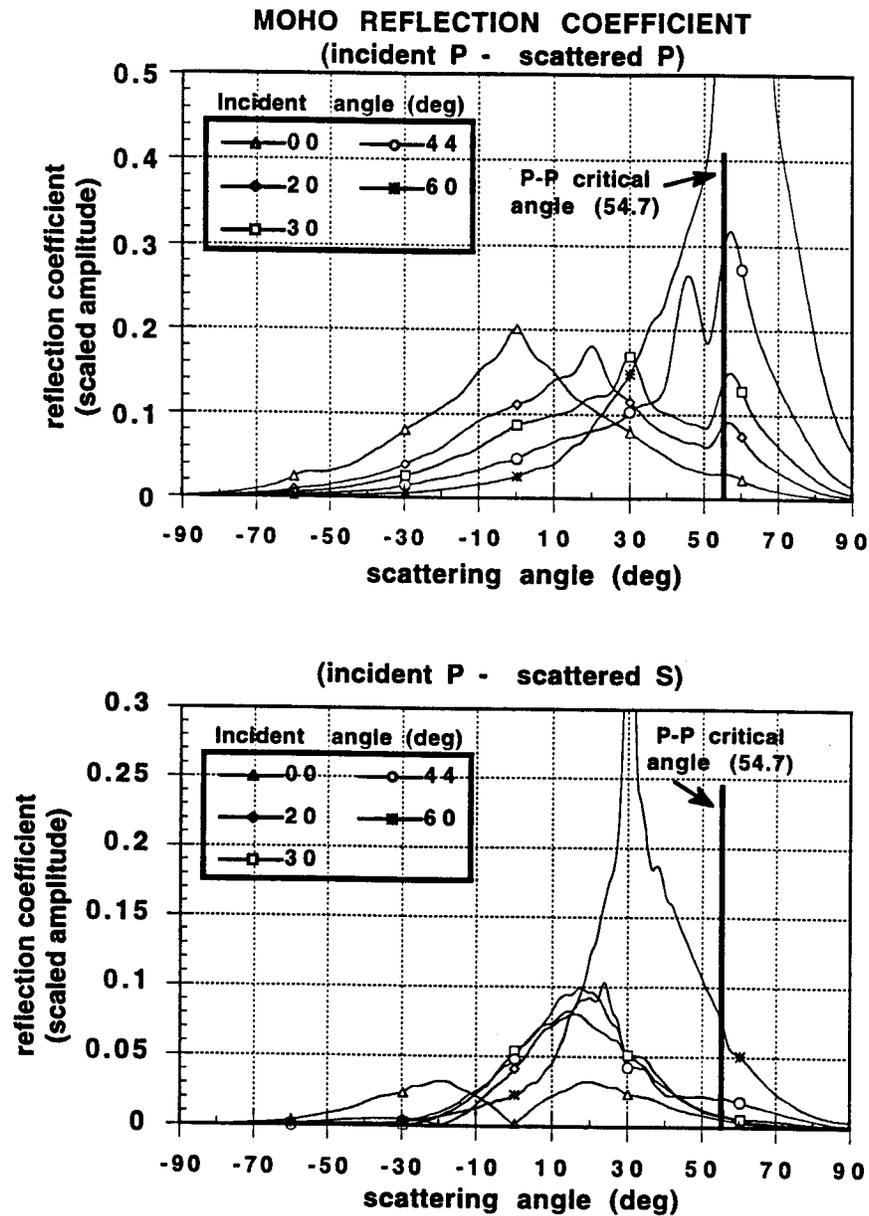
Figure 5: The numerical reflection coefficient calculated over an irregular 2-D Moho discontinuity with an *rms* slope of 10°. The total mean reflection coefficient over a randomly irregular interface with Gaussian properties is given. The S-S critical angle is approximately the same as the P-P critical angle ($\theta_c = 56°$).

67

MOHO REFLECTION COEFFICIENT
**(incident P - scattered P)**

(incident P - scattered S)
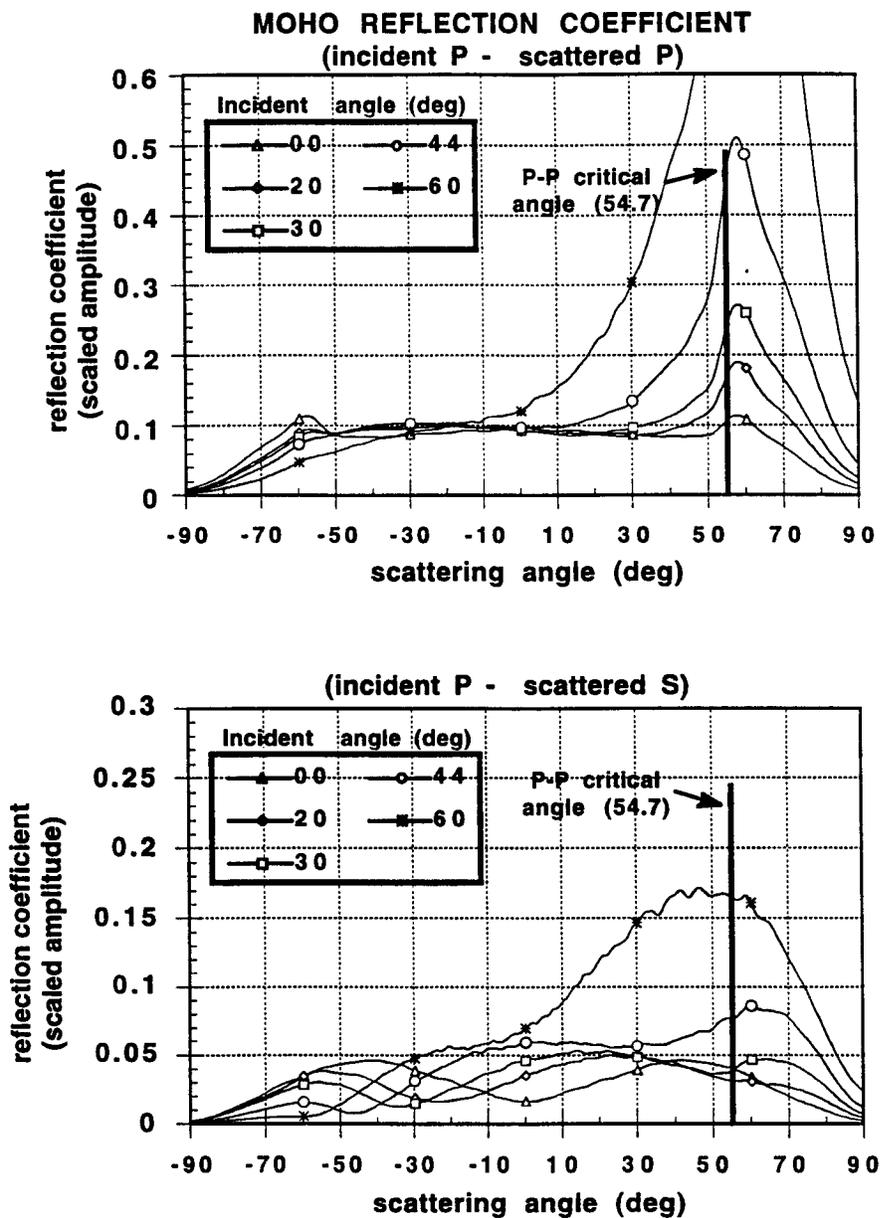
Figure 6: Similar to Figure 5, except for an interface with a 30°.
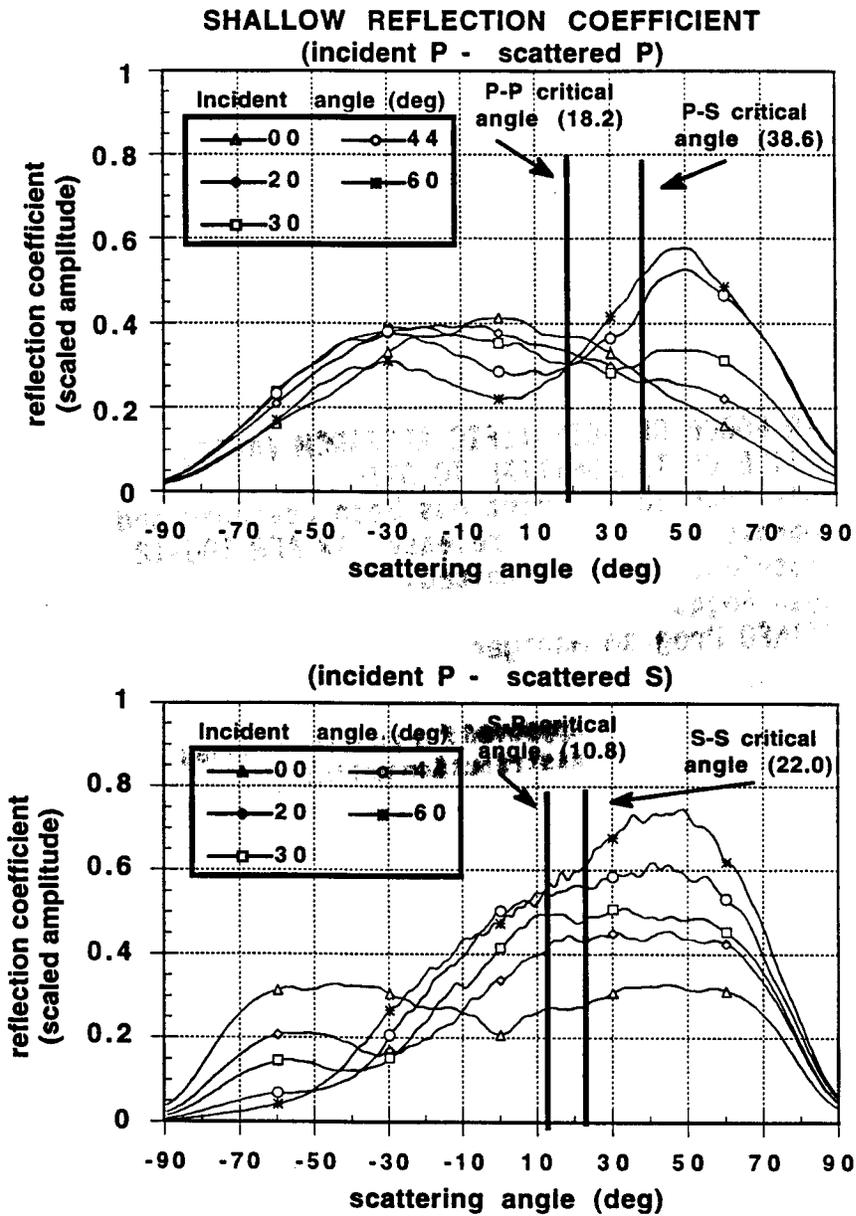
Figure 7: Numerical reflection coefficient calculated over an irregular 2-D soil-basement interface with an *rms* slope of 30°. The total mean reflection coefficient over a randomly irregular interface with Gaussian properties is given.